Research Square

Preprints are preliminary reports that have not undergone peer review.
They should not be considered conclusive, used to inform clinical practice,
or referenced by the media as validated information.

Pressure-Relief Evolution and Lagged Gas-Drainage Response of Protected Seams during Lower Protective Seam Mining in Deep Inclined Coal Seams

Pingdingqi Tuo
China University of Mining and Technology
Hongxing Zhou
zhou12510@126.com

China University of Mining and Technology
Haifeng Wang
China University of Mining and Technology
Cunyang Lu
China University of Mining and Technology
Zhiyuan Wang
China University of Mining and Technology
Zhiyuan Guo
China University of Mining and Technology

Research Article

Keywords: Deep coal seam, Lower protective seam mining, Pressure-relief evolution, Expansion deformation ratio, Gas drainage

Posted Date: July 20th, 2026

DOI: https://doi.org/10.21203/rs.3.rs-10285983/v1

License: This work is licensed under a Creative Commons Attribution 4.0 International License.
Read Full License

Additional Declarations: No competing interests reported.

Version of Record: A version of this preprint was published at Geomechanics and Geophysics for Geo-Energy and Geo-Resources on October 5th, 2026. See the published version at https://doi.org/10.1007/s40948-026-01250-3.

Pressure-Relief Evolution and Lagged Gas-Drainage Response of Protected Seams during Lower Protective Seam Mining in Deep Inclined Coal Seams

Pingdingqi Tuo[a,b,c,d], Hongxing Zhou[a,b,c,d*], Haifeng Wang[a,b,c,d], Cunyang Lu[a,b,c,d], Zhiyuan Wang[a,b,c,d], Zhiyuan Guo[a,b,c,d]

[a]*School of Safety Engineering, China University of Mining and Technology, Xuzhou 221116, China;*

[b]*State Key Laboratory of Coal Mine Disaster Prevention and Control, China University of Mining and Technology, Xuzhou 221116, China;*

[c]*Key Laboratory of Theory and Technology on Coal and Rock Dynamic Disaster Prevention and Control, National Mine Safety Administration, China University of Mining and Technology, Xuzhou 221116, China;*

[d]*National Engineering Research Center for Coal Gas Control, China University of Mining and Technology, Xuzhou 221116, China;*

Abstract: In deep coal seam groups, pressure relief induced by lower protective seam mining does not necessarily lead to synchronous gas-drainage enhancement, making it difficult to define effective protection ranges and drainage timing. This study investigates the mechanical–hydraulic mismatch in the III1022 working face of Luling Coal Mine by integrating FLAC^{3D} numerical simulation, field verification of pressure-relief boundaries, roof–floor deformation monitoring, and surface-borehole drainage data within a unified advance-distance framework. An initial compaction compensation ratio, $C_n(x)$, is proposed to normalize the formation criterion of strong pressure relief by comparing mining-induced expansion release with the initial normal compaction strain of the protected seam. The onset of drainage enhancement is further identified using a continuous piecewise-growth model of the total drainage rate $Q(x)$. Results show that the protected seam exhibits staged and zoned responses. Once established, the strong pressure-relief zone evolves within a finite stable range rather than expanding indefinitely. The criterion $C_n(x)$=1 identifies the onset of strong pressure relief at 128.8 m, with a continuous strong pressure-relief interval of 128.8–1216.6 m. In contrast, working-face-scale drainage enhancement begins at 280.4 m, indicating a spatial lag of 151.6 m. Lag-corrected local

conversion intensity reveals that drainage conversion is highly nonuniform and concentrated in preferential windows. These findings demonstrate that strong pressure relief is necessary but insufficient for effective drainage; hydraulic effectiveness depends on fracture connectivity, pressure-field reorganization, gas-source mobilization, and borehole interception.

Keywords: Deep coal seam; Lower protective seam mining; Pressure-relief evolution; Expansion deformation ratio; Gas drainage

1 Introduction

With increasing mining depth, coal seam groups are increasingly characterized by high in-situ stress, high gas pressure, low permeability, and strong geological heterogeneity, which together intensify the difficulty of gas control and outburst prevention. Under such deep geological conditions, the key challenge is no longer limited to whether mining disturbance can induce pressure relief in adjacent seams, but extends to whether such pressure relief can be effectively transformed into sustained permeability enhancement and efficient gas drainage. In this context, understanding the spatial evolution of mining-induced pressure relief and its coupling relationship with gas drainage is of great significance for both mine safety and efficient gas exploitation (Yuan et al., 2025; IEA, 2024).

Protective seam mining has long been recognized as one of the most effective regional measures for preventing coal and gas outbursts in coal seam groups. Its essential mechanism is that extraction of the protective seam redistributes the surrounding stress field, promotes expansion deformation and fracture development in the protected seam, and consequently enhances permeability and gas drainage capacity. Since the concept was first proposed and applied in underground coal mining, extensive studies have been carried out on its pressure-relief mechanism, permeability response, and engineering applicability (Peng et al.,2022; Ren et al., 1980; Xue et al., 2023; Chen et al., 2025; Wang et al., 2013). These studies have laid an important theoretical and technical foundation for pressure-relief gas control in coal mines.

Previous research has mainly focused on three aspects. First, many studies have examined the redistribution of mining-induced stress and the zoning characteristics of pressure relief in protected seams. Xu et al. (Xu et al., 2023) investigated the stress and permeability evolution of high-gassy coal seams under repeated mining and showed that mining disturbance may induce pronounced staged variations in permeability. Lu et al. (Lu et al., 2024) further demonstrated that the pressure-relief effect of protective layer mining is strongly constrained by stress redistribution and mining geometry. Zhu et al. (Zhu et al., 2025) quantified the reconstruction of mining-induced fracture networks and highlighted the anisotropic nature of mining-enhanced permeability. These studies substantially improved the understanding of the mechanical and structural response of protected seams under mining disturbance, but they were more focused on the evolution of stress and fractures themselves than on the direct field-scale manifestation of drainage enhancement.

Second, a large number of studies have investigated the coupling among stress, deformation, fracture propagation, and permeability evolution in coal. Zhao et al. (Zhao et al., 2025) emphasized that the time dependency of coal permeability plays an important role in gas migration and engineering prediction. Yin et al. (Yin et al., 2015) reported that permeability evolution during protective layer mining is governed by the interaction among stress unloading, coal deformation, and gas infiltration. Bai et al. (Bai et al., 2023) showed that permeability in damaged coal under triaxial loading-unloading conditions evolves nonlinearly and is highly sensitive to the stress path. Jing et al. (Jing et al., 2025) further demonstrated that under true triaxial stress, unloading can induce fracture expansion and exponential permeability enhancement, while the influence of horizontal stress may exceed that of vertical stress. Rong et al. (Rong et al., 2024) found that gas seepage in deep coal under three-dimensional stress exhibits pronounced directional and stage-dependent characteristics. Zhang et al. (Zhang et al., 2025) further quantified the spatiotemporal response of coal permeability and highlighted that permeability evolution is controlled not only by geomechanical effects, but also by the asynchronous redistribution of pressure within the matrix-fracture system. These studies collectively indicate that the

transition from mining-induced pressure relief to effective gas drainage is not instantaneous, but is essentially a progressive structural-hydraulic evolution process.

Third, permeability evolution itself, recent studies have also examined the structural basis and engineering implications of pressure-relief effects in protected seams. Yang et al. (Yang et al., 2022) showed that protective seam mining can significantly alter the pore structure of the overlying coal seam, indicating that mining-induced pressure relief is accompanied by persistent microstructural reorganization. Wang et al. (Wang et al., 2020) proposed a safety strategy for deep and thick coal seams based on soft-rock protective layer mining, while Jin et al. (Jin et al., 2016) evaluated the gas-control effectiveness of remote lower protective seam mining in a typical engineering case. Wang and Wang (Wang et al., 2021) further analyzed the seepage characteristics and fracture development of protected seams caused by mining of protecting strata. At the same time, Kan et al. (Kan et al., 2025) demonstrated experimentally that coal permeability evolution under coupled mining disturbance and gas extraction conditions is strongly path-dependent. Zhao et al. (Zhao et al., 2023), Danesh et al. (Danesh et al., 2017), and Wang et al. (Wang et al., 2023) further showed that creep-seepage behavior, time-dependent damage accumulation, and the mechanical response of coal-rock combinations can all influence permeability evolution and flow performance. These findings suggest that the effectiveness of pressure-relief gas drainage depends not only on the occurrence of unloading, but also on the progressive maturation of pore-fracture connectivity and time-dependent seepage adjustment under coupled mining and drainage conditions.

In addition to field and engineering studies have assessed the protection effect of lower protective seam mining using indicators such as residual gas pressure, residual gas content, permeability coefficient, and drainage performance. Previous studies have discussed unloading-induced damage in deep seams (Lv et al., 2025), permeability distribution in protected coal during unloading (Cai et al., 2019), and protection effectiveness under complex geological conditions (Liu et al., 2025). Additional work has examined optimal pressure-relief gas extraction technologies (Ye et al., 2025),

gas extraction and emission laws in protective seams (Wang et al., 2013), and the role of high annular fissure bodies in low-permeability coal seam groups (Sun et al., 2024). These studies provided important practical evidence for evaluating protected seam pressure relief, but most existing evaluations remain focused either on the mechanical response of the coal mass or on the final drainage outcome. The direct spatial correspondence between pressure-relief evolution and drainage enhancement has therefore not been sufficiently clarified.

At present, one major limitation in related studies lies in the inconsistency of analytical scales. Numerical simulations usually describe the evolution of stress relief and deformation in the spatial domain or in terms of face advance distance, whereas field drainage data are commonly recorded in the time domain. This mismatch makes it difficult to directly identify when and where pressure relief becomes hydraulically effective, thereby obscuring the spatial lag that may exist between structural response and drainage enhancement. For deep lower protective seam mining with large interlayer spacing, this issue becomes even more prominent, because the transmission of mining-induced disturbance is weaker and more heterogeneous, while the compact structure and low initial permeability of deep coal seams make the hydraulic response more likely to lag behind the mechanical response (Zhao et al., 2025; Jing et al., 2025; Rong et al., 2024; Lv et al., 2025).

In summary, existing studies have extensively examined the pressure-relief behavior, deformation characteristics, and drainage performance of protected seams during protective seam mining. However, the spatial correspondence between pressure-relief evolution and drainage response remains insufficiently resolved, and a unified-scale method for direct comparison and quantitative analysis is still lacking. In engineering practice, absolute expansion-deformation thresholds are commonly used to evaluate the pressure-relief degree of protected seams, but such thresholds are strongly affected by burial depth, coal stiffness, seam thickness, in-situ stress, and interlayer structure, and are therefore difficult to generalize across different mines. Accordingly, this study takes the III1022 working face of Luling Coal Mine as the engineering background and, based on numerical simulation, field investigation, and drainage data analysis, adopts a

same-scale advance-distance framework to investigate the relationships among pressure-relief evolution, expansion deformation, and gas-drainage response in the protected seam. An initial compaction compensation ratio is further introduced to convert the absolute expansion-deformation threshold into a structural-weakening criterion relative to the initial compaction state of the coal seam, thereby reducing dependence on a single empirical threshold.

2 Background and Theoretical Framework

2.1 Geological setting and study background

The Luling Coal Mine is located in Anhui Province, China, approximately 20 kilometers southeast of Suzhou City. Fig. 1 provides details on the mine's location and strata. The shallow boundary of the minefield is controlled by the outcrop of Coal Seam No. 10, whereas the deep boundary is defined by the -800 m contour of Coal Seam No. 8. The minefield is approximately 8.2 km long along strike and 3.6 km wide along dip, covering an area of about 19.0894 km^2. Overall, the mine has complex geological structures and well-developed faults, which pose major challenges to safe and efficient deep mining and gas control.

Eight mineable coal seams, numbered 3, 4, 5, 6, 7, 8, 9, and 10, occur in the study area. Stratigraphically, Coal Seam No. 10 lies below Coal Seams No. 8 and No. 9 and serves as the protective seam in this study. In the III2 mining district, the interburden between Coal Seams No. 10 and No. 9 ranges from 63.94 to 105.63 m, with an average of 76.19 m, whereas the spacing between Coal Seams No. 8 and No. 9 ranges from 1.03 to 4.95 m, with an average of 2.49 m. Thus, Coal Seams No. 8 and No. 9 form a close-distance seam group, while Coal Seam No. 10 and the overlying protected seams represent a typical large-interburden lower protective seam mining condition. This seam configuration leads to marked attenuation during upward transmission of mining disturbance and makes the case representative for the present study.

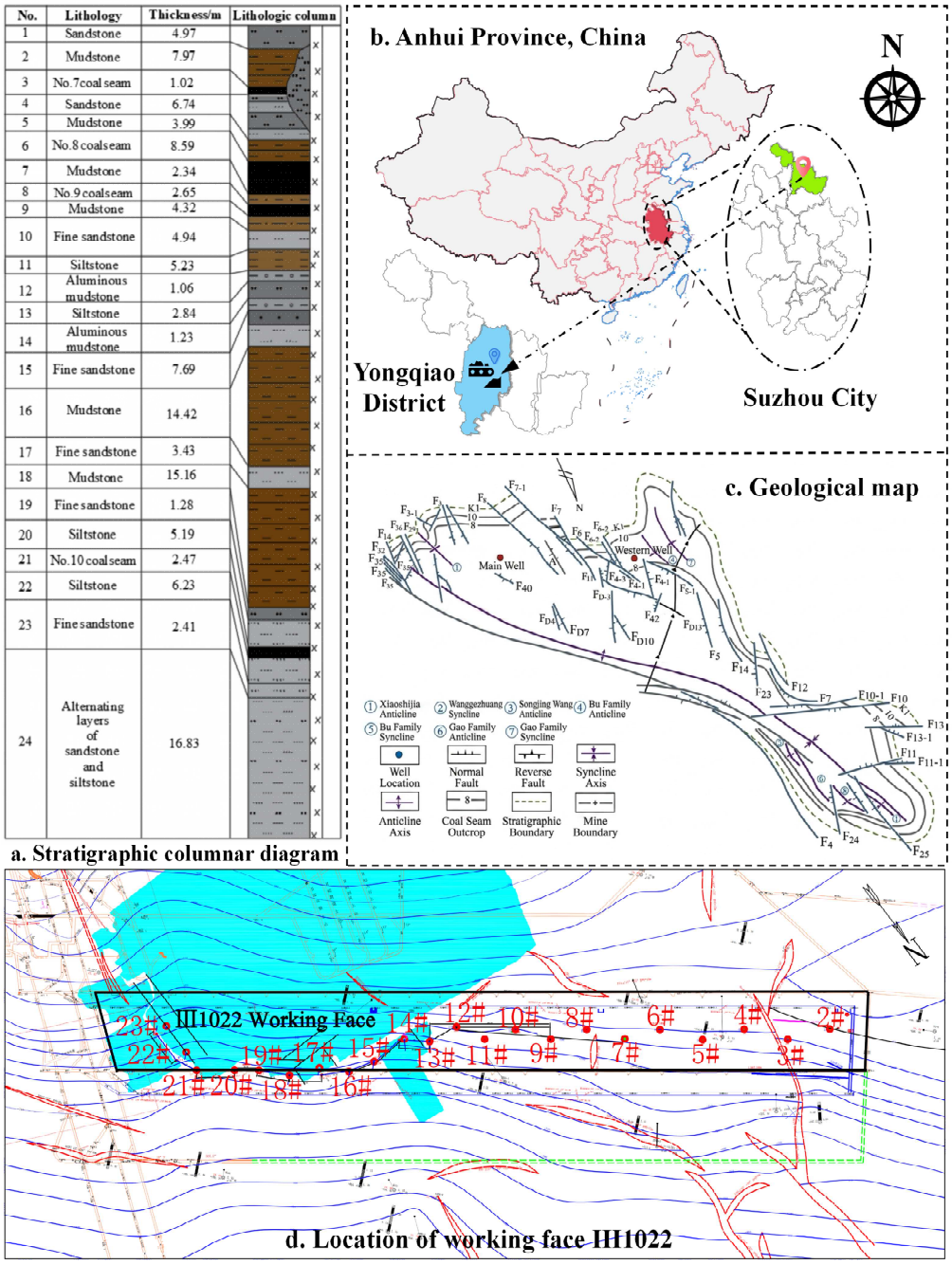


Fig. 1. Geological and engineering setting of the study area: (a) stratigraphic columnar diagram of the coal-bearing sequence; (b) regional location of Luling Coal Mine in Anhui Province, China; (c) geological map of the mine field; and (d) layout of the III1022 working face.

Luling Coal Mine is an outburst-prone mine, and Coal Seams No. 8, No. 9, and No. 10 all present coal and gas outburst hazards. For Coal Seam No. 8, the adsorption constants are a=20-39 m^3/t and b=0.2-0.5 MPa^{-1}, indicating strong adsorption capacity. At the -882 m level, the maximum gas pressure and gas content of Coal Seams No. 8 and No.

9 reach 5.0 MPa and 25 m^3/t, respectively. The firmness coefficient ranges from 0.11 to 0.46, with an average of only 0.26, indicating extremely soft coal. The permeability coefficient is only 2.8 x 10^{-2} m^2/(MPa^2.d), and the initial gas-flow velocity in boreholes is 17-30 ml/s. These parameters indicate that Coal Seams No. 8 and No. 9 have high outburst risk and low initial permeability. Direct drainage under conventional conditions is therefore ineffective, and pressure-relief permeability enhancement induced by protective seam mining is required.

In the III1 mining district, the maximum gas pressure and gas content of Coal Seam No. 10 at the -801 m level reach 3.8 MPa and 17.9 m^3/t, respectively. Its adsorption constants are a=15.25-29.83 m^3/t and b=0.41-1.3 MPa^{-1}, and its firmness coefficient is 0.8-1.13. Although Coal Seam No. 10 has better coal properties than Coal Seams No. 8 and No. 9, it remains a gas-bearing outburst-prone seam. The study area therefore represents typical complex deep conditions: the lower protective seam itself contains considerable gas, whereas the overlying protected seams form a close-distance seam group with high outburst risk and poor drainability.

The field test was conducted at the III1022 fully mechanized working face in Coal Seam No. 10. This working face is located in the III2 mining district, adjacent to the III4 mining district to the west, bounded by the protection-pillar line of the main entries in the III2 mining district to the east, adjacent to the II104 mining district to the south, and adjacent to the III1024 working face to the north. The designed strike length, dip length, and mining area of the working face are 1436 m, 170 m, and 239231 m^2, respectively. The seam dip ranges from 13 deg to 28 deg, with an average of 17 deg.

2.2 Theory of pressure relief and gas-drainage response in protected seams

2.2.1 Research Strategy and Basic Assumptions

After lower protective seam mining, the protected seam undergoes stress redistribution, accompanied by fracture opening, coal expansion deformation, and changes in seepage capacity. Under field conditions, fracture aperture and in-situ permeability cannot be continuously measured, whereas roof-floor displacement and seam deformation can be obtained more readily from numerical simulation and field monitoring. From an engineering perspective, this study uses

160 macroscopic deformation to characterize structural changes within the seam, represents seam expansion by the
161 roof-floor displacement difference of the protected seam, and further introduces the compaction compensation ratio
162 Cn(x) and its variation with advance distance to analyze the relationships among mining-induced pressure relief,
163 structural relaxation of coal, and gas-drainage response.

164 The following assumptions are adopted for the subsequent analysis:

165 (1) The protected seam is treated as a fractured continuum, and its macroscopic seepage capacity is governed
166 mainly by fracture development and connectivity.

167 (2) Coal deformation induced by protective seam mining involves elastic deformation, creep deformation, and
168 desorption-induced shrinkage, but the dominant factor controlling permeability improvement is fracture propagation
169 and coalescence.

170 (3) Within the borehole influence range, gas flow can be approximated by Darcy-type seepage at the engineering
171 scale, and drainage intensity is controlled mainly by the equivalent permeability and pressure gradient of the coal seam.

172 (4) Mining-induced effects evolve in stages as the working face advances; therefore, the pressure-relief indicators
173 obtained from numerical simulation and the drainage parameters recorded in the field are both expressed as functions of
174 working-face advance distance. The time-to-advance-distance conversion method is given in Section 2.2.2.

175 2.2.2 Same-scale transformation in the advance-distance domain

176 Pressure-relief indicators obtained from numerical simulation, such as stress, displacement, and expansion
177 deformation ratio, are naturally expressed as functions of working-face advance distance or spatial position, whereas
178 field gas-drainage data are usually recorded as time series. If drainage is analyzed in the time domain while
179 pressure-relief evolution is analyzed by advance distance, their spatial correspondence cannot be determined directly.
180 Therefore, the field drainage data are transformed from the time domain to the working-face advance-distance domain
181 to enable same-scale comparison between pressure-relief indicators and drainage response.

Let x denote the cumulative advance distance of the working face measured from the open-off cut. The advance distance can be expressed as:

$$x = X(t) = X(t_0) + \int_{t_0}^{t} v_f(\tau)\mathrm{d}\tau \quad (1)$$

where $X(t_0)$ is the working-face position at the initial time, t_0 is the initial mining time, and $v_f(\tau)$ is the instantaneous advance speed. For discrete field records, the equation can be written as:

$$x_i = X(t_i) = X(t_0) + \sum_{n=1}^{i} v_f(t_n)\Delta t_n \quad (2)$$

where x_i is the cumulative advance distance corresponding to the ith drainage record, andΔt_n is the time interval between adjacent records. If the daily working-face position is recorded in the field, x_i can be determined directly from the measured advance position.

The seepage capacity of a coal seam is controlled by fracture aperture, fracture density, fracture connectivity, and flow-path stability (Harpalani et al., 1995; Liu et al., 2019). The gas-drainage rate recorded in the time domain can therefore be transformed into the advance-distance-domain drainage response as follows:

$$Q(x_i) = Q(t_i), x_i = X(t_i) \quad (3)$$

where $Q(t_i)$ is the total gas-drainage rate recorded at time t_i. If multiple boreholes or drainage methods are considered, the total working-face-scale drainage response can be written as:

$$Q(x_i) = \sum_{j=1}^{N} q_j(x_i) \quad (4)$$

where $q_j(x_i)$ is the drainage rate of the jth borehole or the jth drainage system at advance distance x_i.

After this transformation, the gas-drainage response $Q(x)$ can be compared under the same advance-distance coordinate. This treatment reduces the effect of changes in working-face advance speed on time-series drainage data and allows the formation position of strong pressure relief, the onset of significant drainage enhancement, and the lag distance between them to be identified in a unified advance-distance domain.

2.2.3 Macroscopic characterization of expansion deformation

Under small-strain conditions, the volumetric strain of coal can be expressed as the sum of the three principal strains (Yin et al., 2015; Danesh et al.,2017) :

$$\varepsilon_v = \varepsilon_1 + \varepsilon_2 + \varepsilon_3 \tag{5}$$

where ε_v is the volumetric strain, and ε_1, ε_2, and ε_3 are the three principal strains. For deep coal masses, the total strain generally consists of elastic strain, time-dependent creep strain, and matrix shrinkage strain associated with gas desorption, and can therefore be further written as:

$$\varepsilon_{ij} = \varepsilon_{ij}^{e} + \varepsilon_{ij}^{v} + \varepsilon_{ij}^{s} \tag{6}$$

where ε_{ij}^{e} is the elastic strain component, ε_{ij}^{v} is the viscoelastic or creep strain component, and ε_{ij}^{s} is the desorption-induced shrinkage strain component. The creep–seepage relationship of coal under unloading and gas–solid coupling has been well demonstrated in experimental studies; therefore, Eq. (6) can be regarded as a reasonable basis for analyzing the mining-induced response of deep coal seams (Wang et al., 2023; Wei et al., 2022) .

Because the target seam is inclined, roof-floor separation should strictly be calculated along the seam-normal direction. If the vertical displacement difference between the roof and floor is extracted from numerical simulation or field monitoring, it can be used as an engineering approximation. Let $H_f(x)$ and $H_r(x)$ denote the vertical displacements of the seam floor and roof, respectively, at advance distance x. Taking positive values as roof-floor separation, the vertical separation can be written as:

$$\Delta H(x) = H_f(x) - H_r(x) \tag{7}$$

The vertical expansion deformation ratio is defined as:

$$\gamma_v(x) = \frac{\Delta H(x)}{h_s} \tag{8}$$

where hs is the original seam thickness, and the corresponding variable denotes the engineering equivalent expansion deformation ratio based on vertical roof-floor separation.$\gamma_v(x)$

Taking separation along the seam-normal direction as positive and considering the effect of seam dip angle θ on

the normal separation, the normal expansion deformation ratio can be approximated as:

$$\gamma_n(x) \approx \gamma_v(x)\cos\theta \tag{9}$$

To describe the local trend of expansion deformation along the working-face advance direction, the expansion deformation-ratio gradient is introduced:

$$S_\gamma(x) = \frac{\mathrm{d}\gamma(x)}{\mathrm{d}x} \tag{10}$$

For discrete advance-distance records, it can be approximated using a finite-difference form:

$$S_\gamma(x_i) \approx \frac{\gamma(x_{i+1}) - \gamma(x_i)}{x_{i+1} - x_i} \tag{11}$$

The expansion deformation ratio gamma directly reflects the relative roof-floor separation of the coal seam, but its magnitude is sensitive to seam thickness, coal stiffness, burial depth, initial stress level, and interlayer structure. Direct use of a fixed absolute expansion threshold to evaluate strong pressure relief across different seams or mines may therefore lead to empirical and case-dependent judgments. To reduce this dependence, the expansion release is related to the initial compaction state of the coal seam, and the initial compaction compensation ratio is defined.

Before protective seam mining, the protected seam is in an initial compacted state. After protective seam mining, roof-floor relative separation reflects the release of this initial compaction. Let ε_0 denote the initial normal compaction strain of the protected seam. The initial compaction compensation ratio is defined as:

$$C_n(x) = \frac{\gamma_n(x)}{\varepsilon_{n0}} \tag{12}$$

where $C_n(x)$ denotes the ratio of the actual expansion release of the coal seam to its initial normal compaction strain. When $C_n(x)<1$, the expansion release has not reached the initial compaction strain. When $C_n(x)>=1$, the expansion release has reached or exceeded the initial compaction strain, and the protected seam has the deformation basis required for forming a strong pressure-relief zone.

At the engineering scale, ε_0 can be estimated from the initial stress state and the equivalent compression stiffness of

the coal seam:

$$\varepsilon_{n0} = \frac{|\sigma_{n0}|}{M_c} \tag{13}$$

where:

$$\sigma_{n0} = \mathbf{n}^T \boldsymbol{\sigma}_0 \mathbf{n} \tag{14}$$

where σ_{n0} is the initial normal stress of the protected seam, σ_0 is the initial stress tensor, n is the unit normal vector of the seam, and M_c is the equivalent normal compression modulus of the coal seam. If the coal in the numerical model is represented using equivalent isotropic elastic parameters, M_c can be approximated by the equivalent constrained modulus under one-dimensional strain conditions:

$$M_c \approx K + \frac{4}{3}G \tag{15}$$

where K and G are the equivalent bulk modulus and shear modulus, respectively, assigned to the corresponding coal seam in the numerical model. This expression is derived from the constrained modulus relation for an isotropic linear elastic material and is used only as an engineering-scale estimate of the initial normal compaction strain. For different seams or mining conditions, K, G, and σn0 should be recalculated according to the corresponding mechanical parameters and initial stress state.

Accordingly, the normalized criterion for the formation of strong pressure relief is written as:

$$C_n(x) \geq 1 \tag{16}$$

This condition indicates that the expansion release of the protected seam has reached its initial normal compaction strain. Compared with a fixed absolute expansion threshold, this criterion accounts for both coal stiffness and initial stress state and is therefore more suitable for comparison among different seams.

3 Numerical Modelling of Pressure-Relief Evolution in Protected Seams

3.1 Model Construction and Boundary Conditions

To analyze the pressure-relief response of the protected seam and the subsequent gas-drainage response during

deep lower protective seam mining, a three-dimensional FLAC^{3D} model was established according to the geological conditions of Luling Coal Mine. The model dimensions along strike, dip, and vertical directions are 1500 m, 170 m, and 200 m, respectively. The model contains 29 strata and 2,196,384 grid elements. The dip angle of the coal-rock sequence is 17 deg, consistent with the average seam dip in the study area. The coal and rock strata were represented by a Mohr-Coulomb elastoplastic constitutive model. The required parameters include bulk modulus, shear modulus, cohesion, internal friction angle, and tensile strength, corresponding to the mechanical parameters listed in Table 1. The simulated working face is 1400 m long along strike and 170 m wide along dip. Coal Seam No. 10, the protective seam, is mined at a thickness of 2.5 m as full-seam extraction, whereas the thicknesses of the protected Coal Seams No. 8 and No. 9 are 8.5 m and 2.5 m, respectively (Fig. 2).

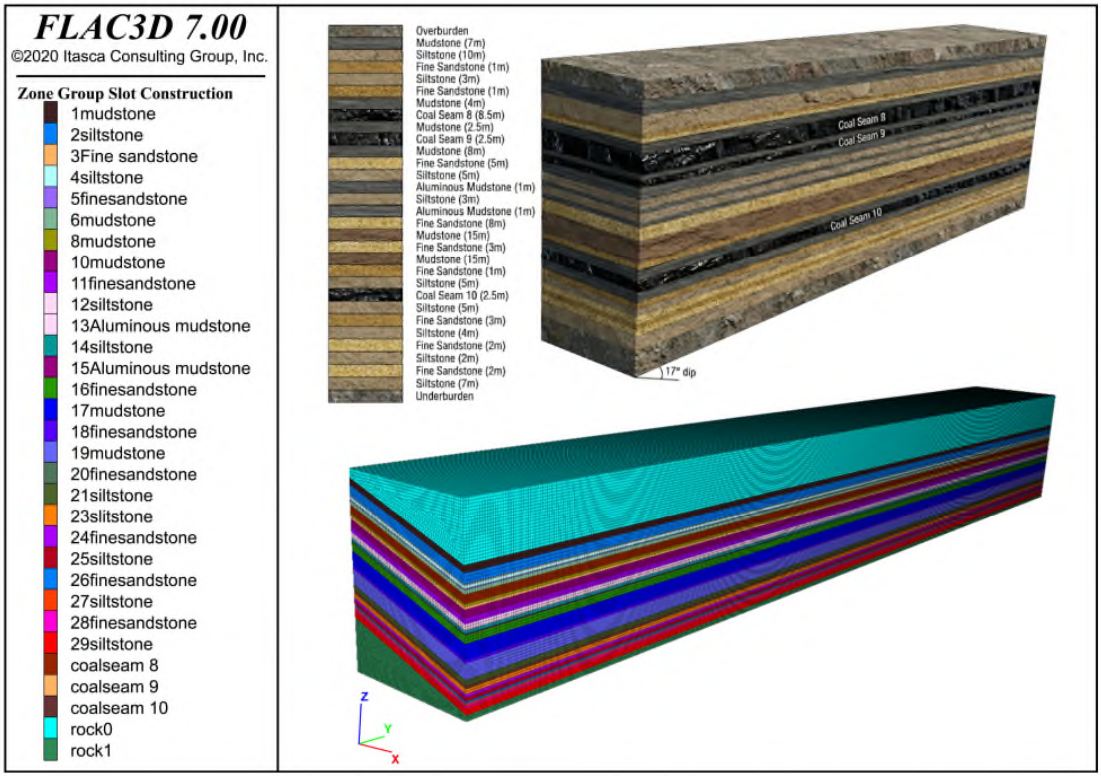


Fig. 2. Model boundary conditions and coal seam excavation location

Rolling constraints are applied to the two lateral boundaries and the bottom boundary. To reproduce the in-situ stress state, a vertical load of 8.32 MPa is applied to the model top together with gravity, with gravitational acceleration set to 9.81 m/s^2. Protective seam mining is simulated by stepwise excavation. Coal Seam No. 10 is advanced by 20 m

per step along strike, and the 1400 m mining length is divided into 70 excavation steps. At each step, the corresponding mining elements are assigned a Null model to represent instantaneous unloading after coal extraction, followed by mechanical equilibrium calculation. To analyze staged evolution of the mining-induced response, stress, displacement, strain increment, and expansion deformation are extracted at advance distances of 100, 200, 300, 400, 600, 800, 1000, and 1400 m.

3.2 Determination of Mechanical Parameters of Rock Strata

The mechanical parameters of the coal-rock strata in the model are mainly determined from the comprehensive stratigraphic column, geological data, and in-situ occurrence conditions of Luling Coal Mine. The parameters include density, bulk modulus, shear modulus, cohesion, internal friction angle, and tensile strength, as listed in Table 1. Individual strata are not assigned separately; instead, the strata are grouped into eight representative lithological categories according to lithology and mechanical parameters. This treatment preserves the basic stratigraphic framework, highlights the dominant factors controlling stress redistribution, coal-seam deformation, and pressure-relief evolution during mining, and improves computational efficiency.

Table 1 Mechanical parameters assigned to the model strata.

No.	Lithology	Density（kg/m^3）	Bulk（GPa）	Shear（GPa）	Cohesion（MPa）	φ/°	Tensile（MPa）
1	Overhanging rock	2580	22.8	18.1	3.5	32	6.8
2	Fine sandstone	2580	24.4	21.6	3.2	33	7
3	Mudstone	2500	10.7	7.9	1.2	32	2.5
4	Coal Seam No. 8	1460	1.74	0.83	1.27	29	0.62
5	Coal Seam No. 9	1380	1.3	0.58	1.25	28	0.64
6	Aluminous mudstone	2467	7.9	6.3	2.16	32	3
7	Siltstone	2564	42.5	25.8	2.75	31	8
8	Coal Seam No. 10	1460	1.98	0.94	1.31	30	0.69

The lithological assemblage of deep coal-bearing strata is complex, and local failure is jointly affected by interlayer differences, primary structures, and mining disturbance. It is difficult to identify mesoscopic fracture parameters for each stratum under field conditions.

The numerical model is calibrated using field pressure-relief boundaries and expansion-deformation monitoring results, as discussed in Section 4.2. The comparison shows that the simulated expansion deformation ratio of the protected seam agrees well with field measurements in Coal Seam No. 9, and that the strong pressure-relief range is generally consistent with the field pressure-relief boundaries determined from residual gas pressure and residual gas content. The model therefore captures the main structural response characteristics of the protected seam during deep lower protective seam mining and can be used for subsequent analysis of pressure-relief evolution and gas-drainage response.

3.3 Response evolution of the protected seam

3.3.1 Stress evolution in the protected seam

Under deep inclined conditions with large interburden spacing, the interlayer structure is complex and protective seam mining shows clear staged behavior. As shown in Fig. 3, the protected seam exhibits a strike-direction stress zoning pattern characterized by front stress concentration, central pressure relief, and rear adjustment. When the working face advances by 200 m, stress reduction has already occurred within approximately 230 m ahead, local pressure relief appears in the 30-230 m range, and the region beyond 230 m remains close to the original stress state. The front concentration zone maintains stress continuity during the transition from the pre-mining to the post-mining load-bearing system, while the central low-stress zone is not yet sufficient to support the formation of a strong pressure-relief zone. During 200-400 m of advance, the low-stress region appears as discontinuous patches and the coal seam remains strongly constrained. During 600-800 m of advance, a continuous low-stress region develops and a regional pressure-relief structure is basically established. After the advance exceeds 1000 m, the overall stress-field pattern becomes stable, and subsequent changes are mainly reflected by strike-direction migration of the pressure-relief zone rather than further enlargement of its core range. The evolution of the strong pressure-relief zone is therefore closer to overall migration after core stabilization than to continuous expansion with advance distance.

On the down-dip side, the angle between the stress-rotation direction and the bedding plane is more favorable for inducing bedding-parallel shear failure. Compared with the compressive state on the up-dip side, this shear failure can overcome coal-rock cohesion earlier and generate a larger mining-induced tensile fracture zone. From an energy-release perspective, the down-dip side occupies a favorable position for gravitational potential-energy release. The elastic energy released by mining not only drives rock failure but is also transformed through interlayer sliding work. This additional work promotes deeper microfracture propagation in the coal mass, resulting in a steeper reduction of lateral confinement on the down-dip side than on the up-dip side.

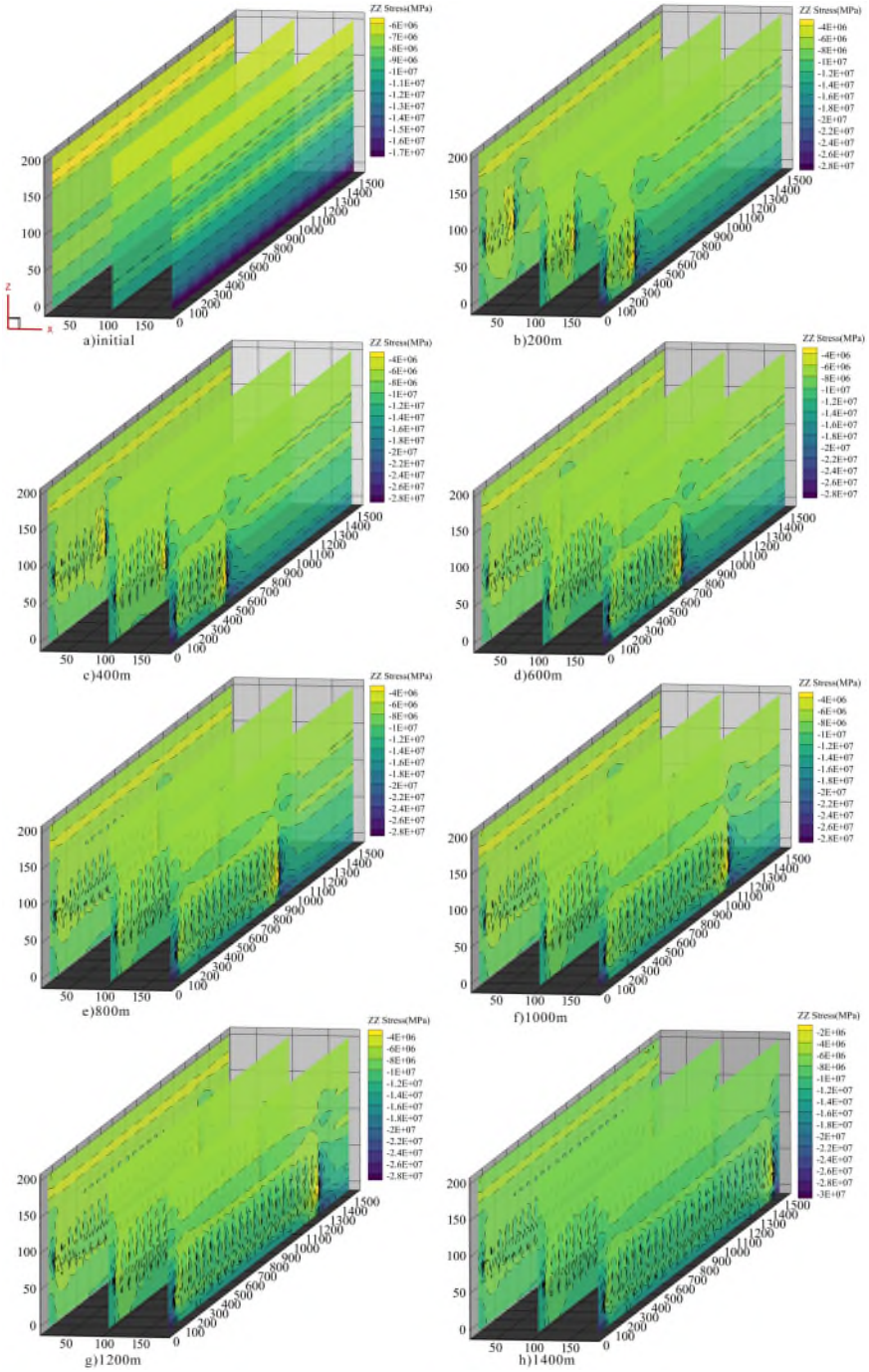


Fig. 3. Evolution of vertical stress in the protected seam during protective seam mining

To further reveal the spatial evolution of the stress field in the protected seam, Fig. 4 presents the three-dimensional Z-direction stress structures of Coal Seams No. 8 and No. 9 at different advance distances. At advances of 200-400 m, low-stress regions have developed in the middle of both seams, but their spatial extents are limited and no continuous pressure-relief belt has formed along strike or dip. The stress-transfer relationship between

the front concentration zone and the rear load-recovery zone remains intact, and the central relief zone is still constrained. After 600-800 m of advance, the low-stress region expands simultaneously along strike and dip and changes from local patches to a continuous spatial distribution. The boundaries between the central relief zone and the front and rear load-bearing zones become clearer, indicating that regional pressure relief has been basically established. The continuity and stable boundary of the low-stress region are key conditions for the formation of strong pressure relief, and a strong pressure-relief zone develops in the central region.

After the advance distance exceeds 1000 m, the pressure-relief range in Coal Seams No. 8 and No. 9 becomes basically stable. The pressure-relief zone then migrates forward along strike with the working face, while the width and spatial control range of the low-stress body change only slightly. Under deep large-interburden conditions, the strong pressure-relief zone has a relatively stable controlling range after formation; continued advance of the working face corresponds to migration of the pressure-relief position, not continuous expansion of the pressure-relief range.

The three-dimensional stress-structure evolution of Coal Seams No. 8 and No. 9 shows marked similarity. Both seams consistently exhibit a spatial pattern of front concentration, central pressure relief, and rear stabilization, indicating that the basic organization of stress redistribution is preserved during upward transmission of mining influence. The low-stress zone forms earlier and covers a larger range in Coal Seam No. 9, whereas the response of Coal Seam No. 8 is relatively delayed. This indicates that interburden distance mainly affects the efficiency and timing of pressure-relief formation but does not change the basic process. The seam closer to the protective seam first reaches a continuous pressure-relief state, followed by the upper seam through the same evolutionary process.

In summary, under deep large-interburden conditions, formation of strong pressure relief in the protected seam requires clear spatial structural conditions. Local low-stress occurrence indicates that mining influence has arrived; formation of a continuous low-stress zone marks the establishment of strong pressure relief; and forward migration of the low-stress body indicates the stable evolution stage of strong pressure relief.

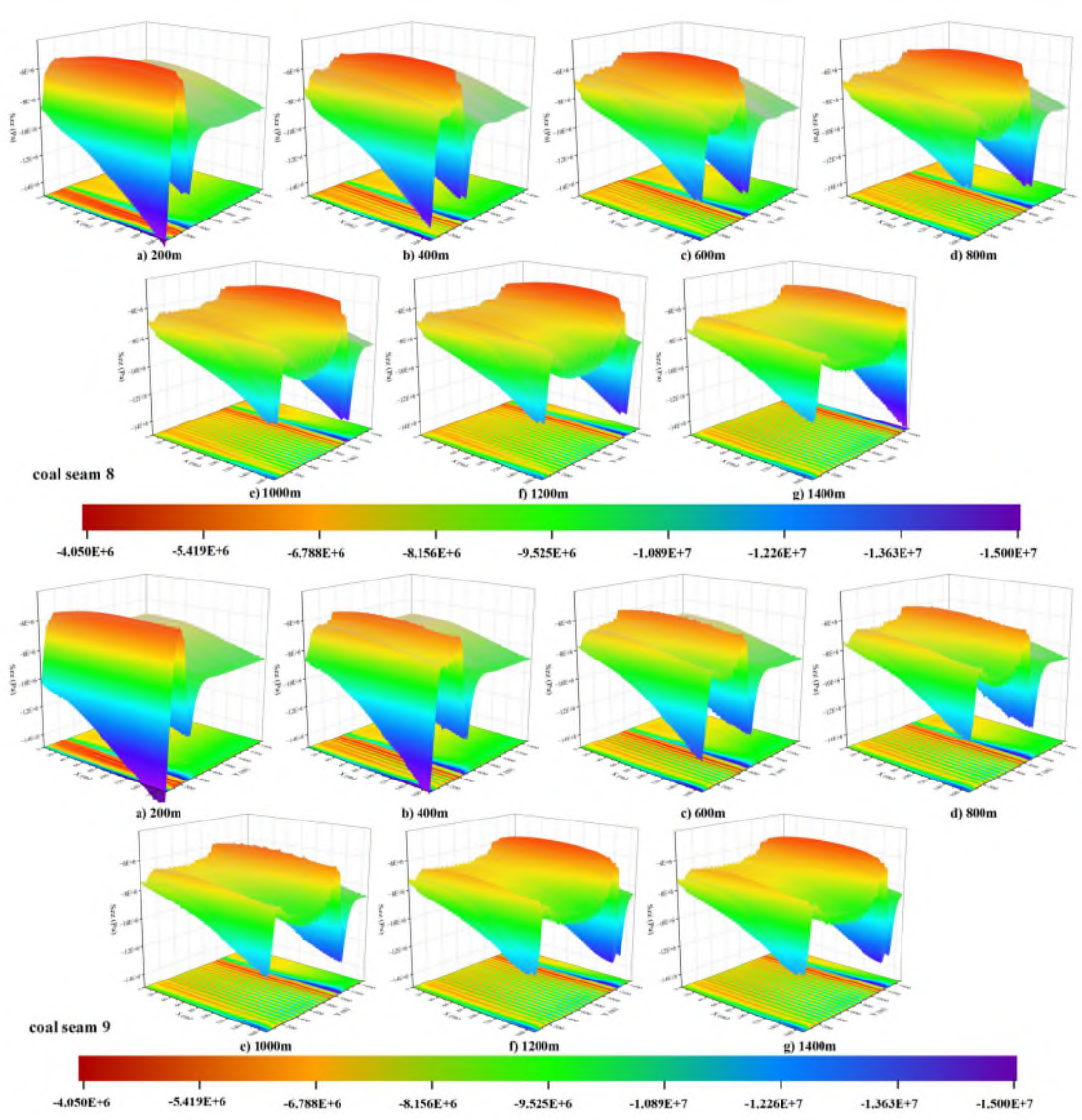


Fig. 4. Three-dimensional evolution of Z-direction stress structures in Coal Seams No. 8 and No. 9 at different advance distances

A monitoring line was arranged along strike at the mid-dip position of Coal Seam No. 8 to record vertical stress when the working face advanced by 100, 200, 300, 400, 600, 800, 1000, and 1400 m. The results are shown in Fig. 5. When the working face advanced to about 600 m, the vertical stress decreased from the original 15.2 MPa to about 2.1 MPa, corresponding to a pressure-relief magnitude of about 87%. Once this stress reduction level was reached, fracture propagation in the coal seam had the conditions for sustained development, and pressure relief began to promote permeability enhancement. Thereafter, the stress reduction changed only slightly, while the pressure-relief range

continued to advance forward.

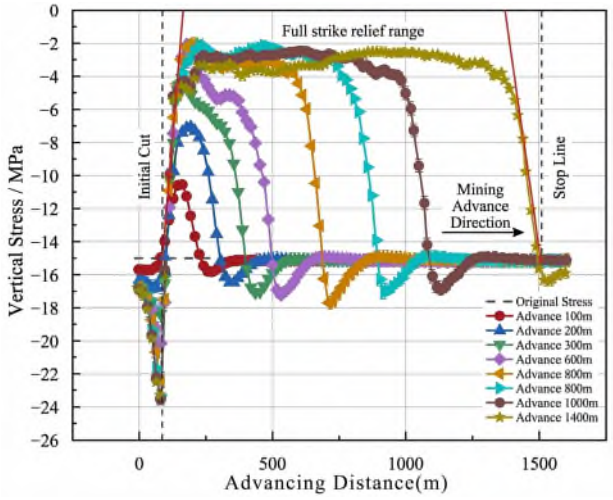


Fig. 5. Variation of vertical stress along the strike direction in the protected seam

Fig. 6 shows the vertical stress distribution along the dip direction on the centerline of Coal Seam No. 8 at different advance distances. The central pressure-relief zone deepens continuously with increasing advance distance. After entering the strong pressure-relief stage, the pressure-relief core is largely established, and subsequent changes are concentrated in minor boundary adjustments. The two lateral boundaries evolve asynchronously: the effective pressure-relief range extends inward by about 21 m on the transport-roadway side and by only about 3 m on the return-air-roadway side. Thus, the strong pressure-relief zone is clearly biased toward the transport-roadway side along dip.

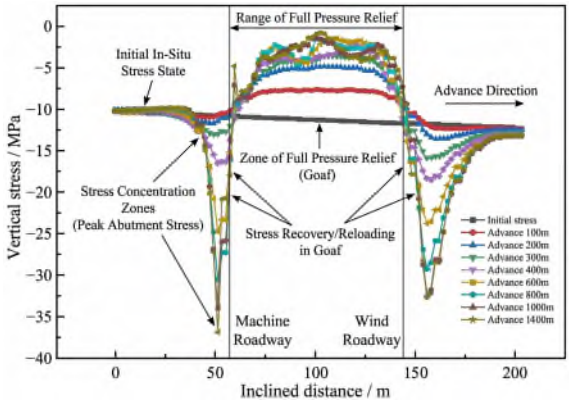


Fig. 6. Vertical stress distribution along the dip direction in the protected seam

The dip-direction boundary controls whether the strong pressure-relief zone can maintain an integral geometry.

After the central low-stress zone reaches a high pressure-relief level, the two side boundaries do not unload synchronously. The belt-conveyor entry side continues to provide space for relief-zone expansion, whereas the return-air entry side enters stress recovery earlier. The strong pressure-relief zone therefore does not expand uniformly from the center; instead, it initiates from the central pressure-relief region, extends toward the favorable side, and terminates earlier on the constrained side. In terms of evolution, dip-direction asymmetry and strike-direction migration jointly determine the spatial position of the strong pressure-relief zone. The strike direction controls when the strong pressure-relief zone forms and how it migrates with face advance, whereas the dip direction controls the lateral extent over which the zone remains continuous.

3.3.2 Displacement and strain-increment evolution in the protected seam

Fig. 7 shows the evolution of the vertical displacement field in Coal Seams No. 8 and No. 9 at different advance distances. At small advance distances, displacement is concentrated mainly in the local region above the goaf, the affected range is limited, and the seam remains constrained by the original structure. With increasing advance distance, the displacement-affected zone expands continuously along strike, and the displacement contours evolve from localized concentration to broad continuous distribution. The displacement fields of Coal Seams No. 8 and No. 9 remain highly consistent in spatial form. The contour ranges of the two seams correspond closely, and the displacement-affected ranges expand synchronously. During upward transmission of mining influence, the interlayer structure does not change the basic mode of overburden movement. Coal Seams No. 8 and No. 9 remain within the same mining-controlled system, and their displacement fields follow the same spatial evolution pattern. The thin siltstone layer between the two seams does not interrupt the continuity of the mining-induced response, and interlayer coupling remains stable.

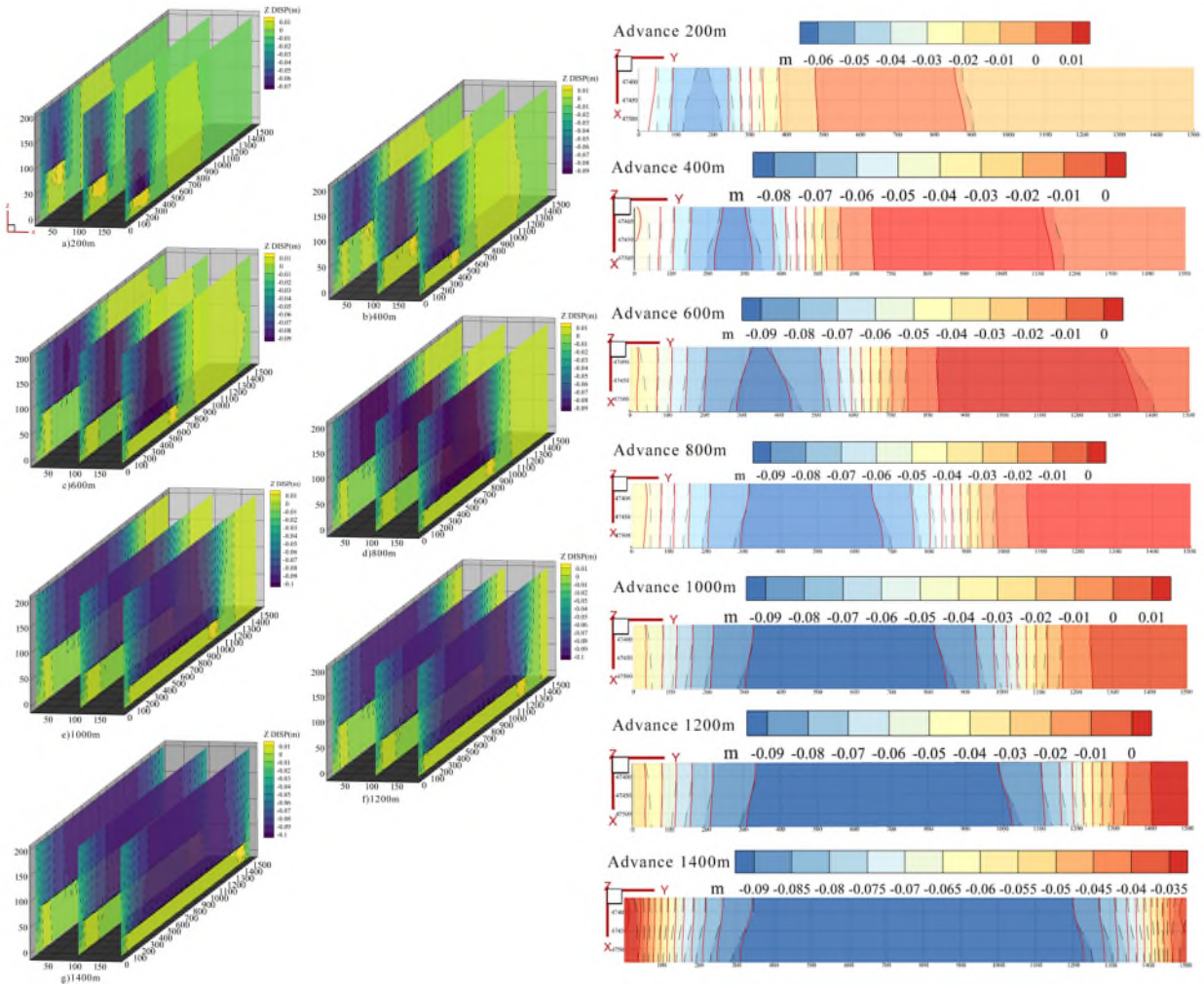
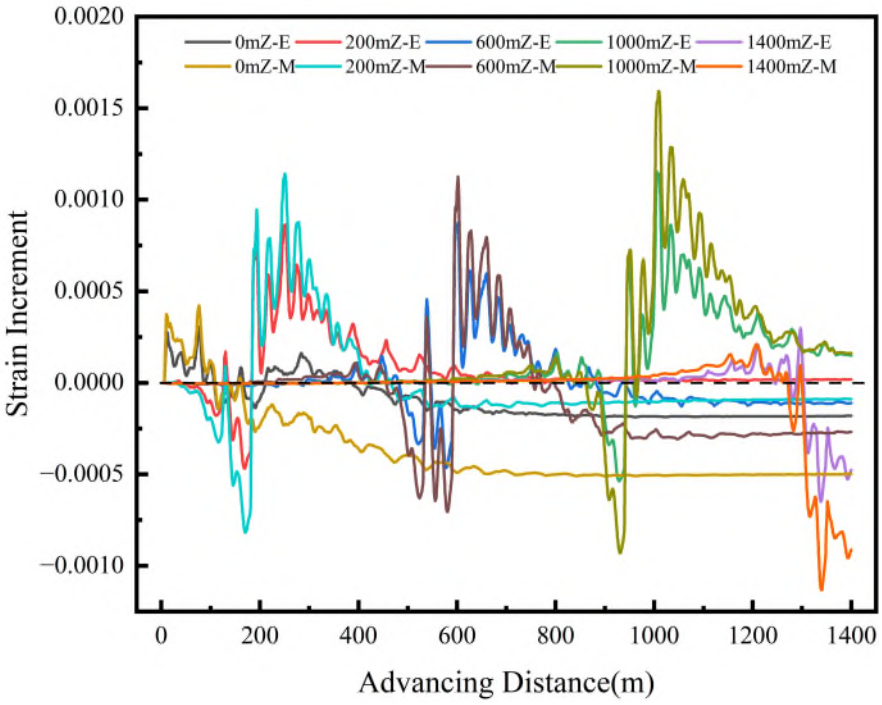


Fig. 7. Evolution of vertical displacement in the protected seam system during protective seam mining

The displacement magnitude and timing show clear stratification. Coal Seam No. 9 consistently has a larger displacement magnitude than Coal Seam No. 8 and enters the pressure-relief stage earlier, whereas the response of Coal Seam No. 8 is delayed. The No. 9 seam, closer to the protective seam, first obtains deformation-release conditions; the upper No. 8 seam responds through the same mechanism but requires a longer transmission path and a larger advance scale. The common origin of the displacement fields and the stratified magnitudes of Coal Seams No. 8 and No. 9 indicate that the upward transmission of mining influence preserves a similar interlayer transfer mode while showing attenuation and lag that increase with interlayer distance. The subsequent strain increment, expansion deformation ratio, and strong pressure-relief criterion are further analyzed on the basis of displacement release.

To identify the staged structural characteristics of the protected seam during mining, Fig. 8 shows the evolution of

409 the Z-direction strain increment with advance distance. The Z-direction strain increment does not accumulate
410 monotonically with advance distance, but exhibits pulse-like fluctuations over several intervals during mining. At small
411 advance distances, the strain increments along all monitoring lines are close to zero, and the seam remains globally
412 constrained. As the working face advances, the strain increment increases rapidly, switches between positive and
413 negative values over short distances, and then decreases again. The Z-direction strain increment records intermittent
414 release of vertical structural constraints within the coal seam, and its peaks correspond to local tensile-strain
415 concentration. Because the initial compaction of deep coal seams is high, fractures cannot propagate continuously at the
416 outset. Structural relaxation therefore occurs through segmented release, and several cycles of local failure and stress
417 reorganization are required before a strong pressure-relief zone forms.



418

419 Fig. 8. Variation of Z-direction strain increment with advance distance

420 The difference between the central and edge monitoring lines reflects the spatial sequence of strong pressure-relief
421 formation. In the central region, Z-direction strain-increment peaks are higher, peak clusters are denser, and
422 concentrated release intervals are shorter, indicating abrupt vertical deformation release. In the edge regions, peak
423 values are lower, fluctuations persist over longer distances, and structural adjustment is more gradual. The central

region is located above the main goaf-controlled area, where differential roof-floor displacement more readily accumulates to a critical state. Vertical tensile failure is more concentrated, and local fractures enter rapid propagation earlier. The edge regions are constrained by residual bearing capacity and boundaries, making high-intensity vertical release difficult; fracture propagation there remains local and discontinuous. Effective pressure relief and permeability enhancement are therefore not established synchronously throughout the seam. A vertical-release-dominated zone first forms in the center and then expands asymmetrically toward the two sides.

Fig. 9 shows the evolution of the Y-direction strain increment with advance distance. Compared with the Z-direction strain increment, the Y-direction increment is smaller overall, its peaks are less concentrated, and it more commonly shows sustained accumulation in the middle and late stages. Early Y-direction response is generally weak, and the seam is dominated by vertical release. In the middle and late advance stages, some monitoring lines develop sustained positive or negative strain accumulation, lateral compression and lateral tension gradually differentiate, and local stress adjustment shifts from single vertical release to dynamic adjustment in the dip direction.

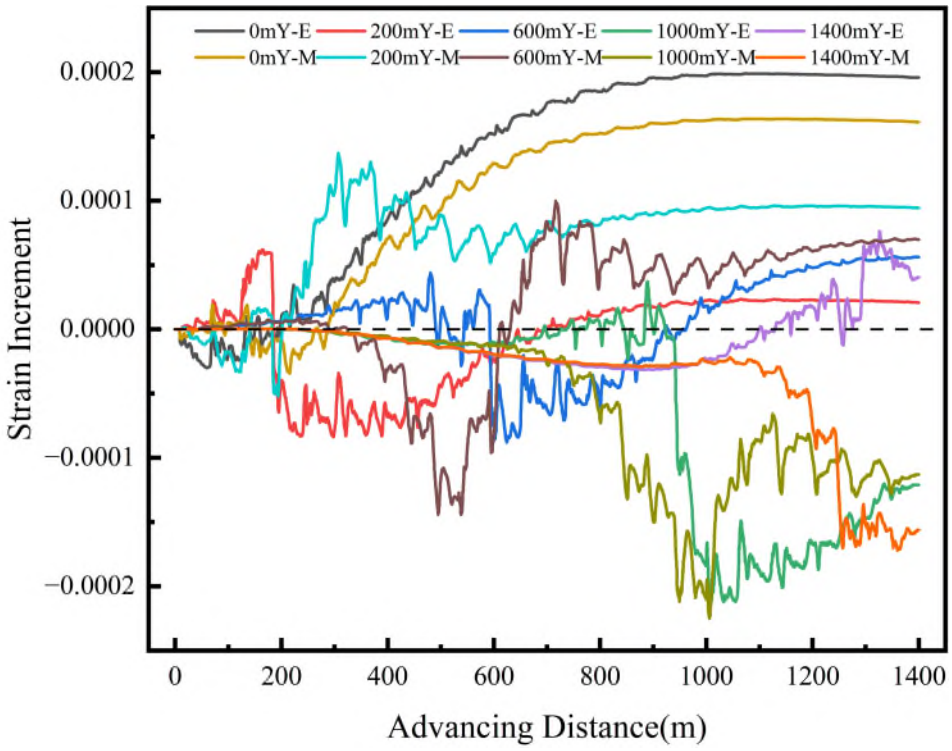


Fig. 9. Variation of Y-direction strain increment with advance distance

In summary, the two sets of strain increments define the sequence of structural evolution in the protected seam. The Z-direction strain occurs earlier and is released more intensively, indicating that vertical release dominates early structural weakening. The Y-direction strain appears later and evolves more gradually, indicating that dip-direction deformation participates in subsequent structural adjustment. Formation of strong pressure relief is not controlled by deformation in a single direction; it first undergoes concentrated vertical release and then gradual dip-direction failure. The deformation-release range of the displacement field and the strain-increment variations jointly determine the spatial evolution of the protected seam.

3.3.3 Evolution of expansion deformation in the protected seam

The preceding stress analysis identifies the formation of a continuous low-stress structure, the displacement field reveals the release of seam movement space, and the strain increments characterize the transition from localized structural release to coordinated deformation. The expansion deformation ratio reflects the roof-floor displacement difference of the protected seam during face advance.

Fig. 10 shows that the expansion deformation remains low during the early advance stage. Although the protected seam has been affected by mining disturbance, structural relaxation is still localized and a continuous pressure-relief structure has not yet formed. At an advance of about 100 m, local gamma exceeds 3 per mille, indicating the emergence of a relaxation zone capable of sustained development. At about 300 m, the spatial outline of the high-gamma zone becomes essentially stable, marking the establishment of the strong pressure-relief core. Thereafter, gamma continues to increase mainly within the established high-value zone, indicating further structural relaxation inside the core. At an advance of 1400 m, the local maximum reaches 19 per mille, with a stable level of about 12 per mille.

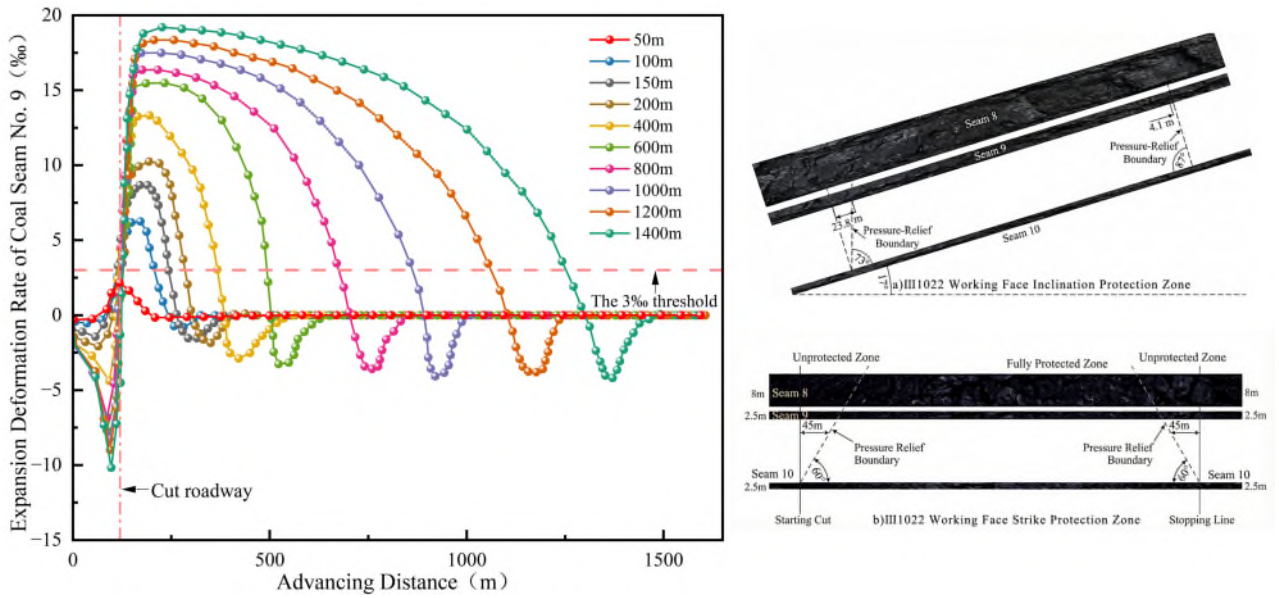


Fig. 10. Distribution of expansion deformation ratio and pressure-relief range in the protected seam

Fig. 10 also shows the late-stage stability of the strong pressure-relief zone. Once the expansion-deformation peak forms, its controlling range rapidly stabilizes. Subsequent advance mainly increases strain release within the core and shifts the overall action position along strike. This behavior is consistent with the three-dimensional stress structure and dip-direction pressure-relief boundary discussed above, indicating that the strong pressure-relief zone has a relatively stable spatial core.

4 Coupled analysis of pressure relief and gas drainage

4.1 Pressure-relief evaluation indicators and criteria

After protective seam mining, the response of the protected seam can be divided into two processes: mining-induced pressure relief, involving stress release, roof-floor separation, and coal expansion deformation; and further fracture connectivity, accompanied by sustained enhancement of gas drainage. This study uses three types of field and simulation indicators to evaluate the protection effect. The first includes residual gas pressure and residual gas content, which verify whether the protected seam satisfies regional outburst-prevention and pressure-relief boundary requirements. The second includes the expansion deformation ratio and the initial compaction compensation ratio, which characterize cumulative deformation release after pressure relief. The third includes gas-drainage rate and its

advance-distance response, which identify the startup, enhancement, attenuation, and competitive diversion of the drainage system.

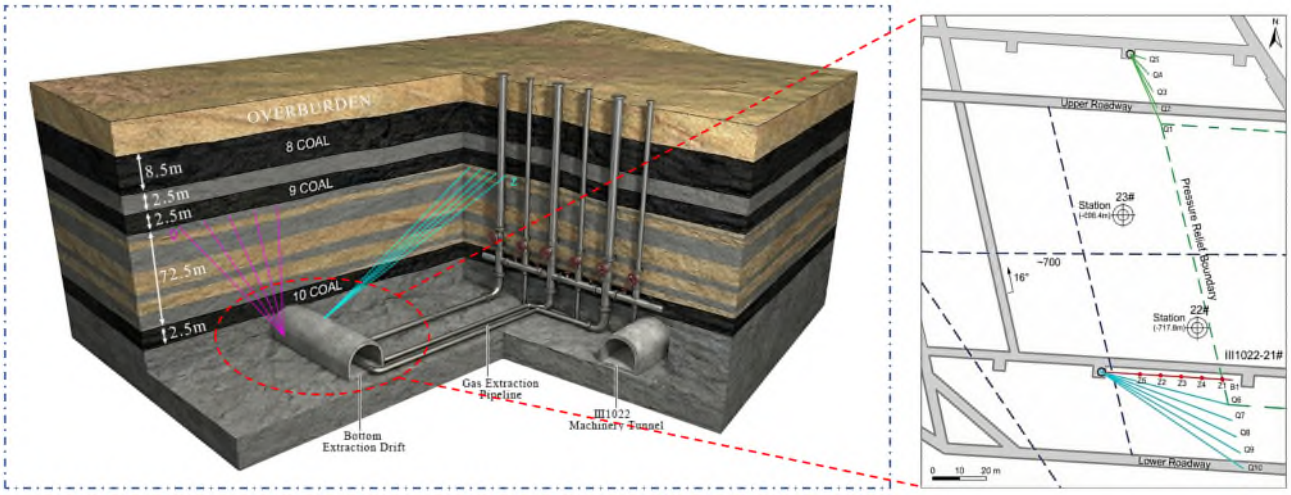


Fig. 11. Layout of field verification boreholes for pressure-relief boundary and expansion-deformation monitoring

The field test boreholes were arranged on both sides of the return-air roadway and transport roadway of the III1022 working face. They included expansion-deformation monitoring boreholes, dip-direction boundary investigation boreholes, and strike-direction boundary investigation boreholes, all passing through Coal Seam No. 9. The layout is shown in Fig. 11. Because the boreholes were deep and borehole deviation was not negligible, all test-point positions were corrected using measured borehole trajectories.

Unlike conventional evaluations based only on residual gas pressure or residual gas content, this study focuses on the spatial correspondence between strong pressure-relief formation and drainage enhancement. Therefore, all field drainage data are transformed into the working-face advance-distance function $Q(x)$ using the method described in Section 2.2.2 and are compared on the same scale with $C_n(x)$ obtained from numerical simulation. This allows the formation position of strong pressure relief and the onset position of significant drainage enhancement to be identified in a unified advance-distance coordinate system.

4.2 Field verification of pressure-relief boundaries

4.2.1 Verification of strike-direction boundary by residual gas pressure and gas content

Fig. 12a shows the residual gas pressure and residual gas content measured in strike-boundary investigation boreholes Z_1-Z_5. The residual gas content ranges from 3.68 to 8.12 m^3/t, and the residual gas pressure ranges from 0.31 to 0.72 MPa. Both increase gradually with distance from the stop line, indicating continuous attenuation of pressure relief along strike. Except for borehole Z_5, where the gas content is close to 8 m^3/t, the residual gas pressure and gas content at the other measuring points are below the outburst-control thresholds, indicating an overall favorable pressure-relief effect along strike. The field-tested boundary extends more than 30 m beyond the range delineated by the regulatory pressure-relief angle, suggesting that the mining influence continues outside the strike boundary.

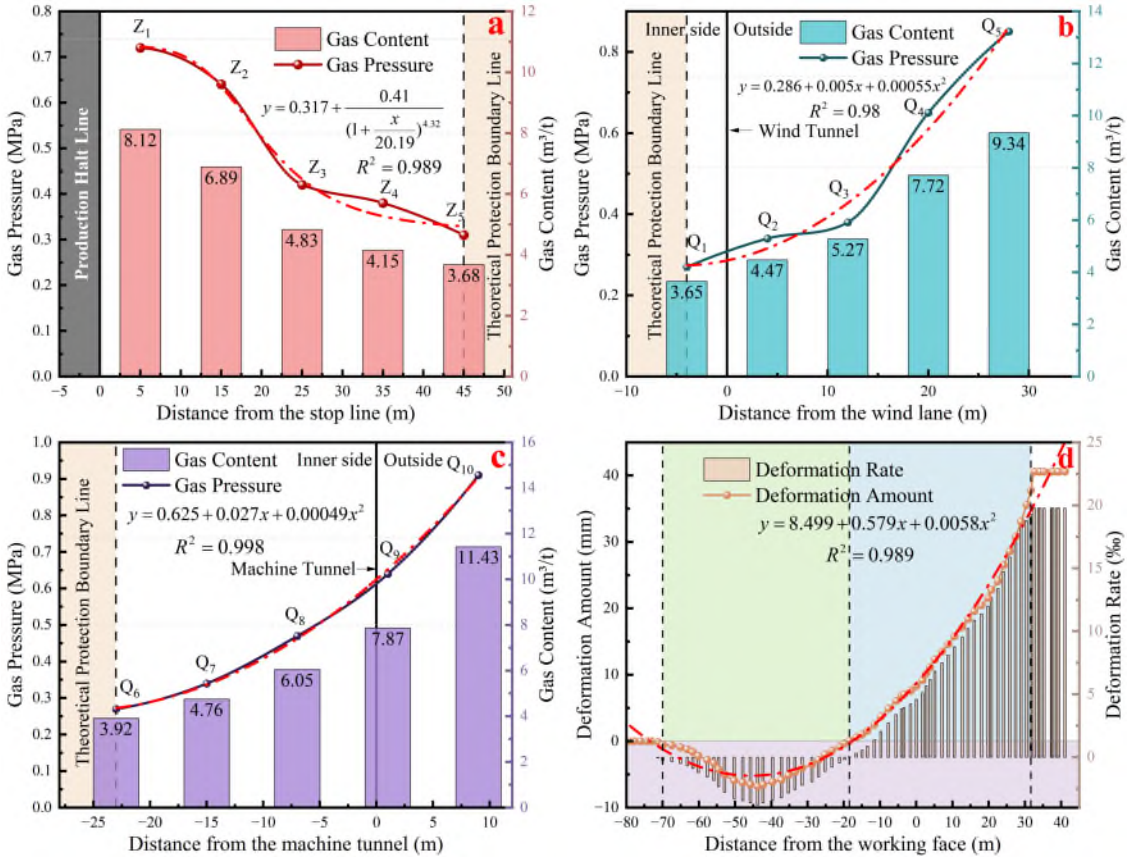


Fig. 12. Field verification of pressure-relief boundary and expansion deformation in the protected seam

Local points outside the boundary that satisfy the gas-pressure and gas-content requirements do not indicate that the entire extended region has formed a stable strong pressure-relief zone. Residual gas indicators reflect the outburst-prevention compliance of local points, whereas the strong pressure-relief zone must be evaluated jointly from stress release, expansion deformation, and spatial continuity.

503 4.2.2 Verification of up-dip and down-dip boundaries

504 Figs. 12b and 12c show the residual gas pressure and gas content measured at the dip-direction boundaries. For the
505 up-dip boundary boreholes Q_1-Q_5, residual gas content is 3.65-9.34 m^3/t and residual gas pressure is 0.27-0.85 MPa; Q_5
506 exceeds the control threshold. For the down-dip boundary boreholes Q_6-Q_{10}, residual gas content is 3.92-11.43 m^3/t and
507 residual gas pressure is 0.27-0.91 MPa; Q_{10} is relatively high. Both up-dip and down-dip sides show an outward
508 increase in gas content and gas pressure, indicating that the dip-direction pressure-relief boundary also has a clear
509 attenuation gradient.

510 The field results are consistent with the asymmetric dip-direction pressure-relief behavior revealed by the
511 numerical simulation in Section 3. The simulation shows that, in inclined seams, the strong pressure-relief zone does
512 not expand symmetrically around the center of the working face, but is jointly controlled by differential roof-floor
513 displacement, interlayer slip, and boundary load recovery. The down-dip side more readily accumulates deformation
514 release and has a relatively larger pressure-relief range, whereas the up-dip side is more strongly constrained by residual
515 bearing capacity and undergoes earlier boundary recovery. The nonuniform attenuation observed on both dip-direction
516 boundaries in the field tests supports this interprŋtion.

517 Accordingly, the dip-direction protection range should not be treated as a simple symmetric boundary. For deep
518 inclined seams, the strike direction controls the formation and migration of the strong pressure-relief zone, whereas the
519 dip direction controls whether the zone remains laterally continuous. The effective protection range should therefore
520 account for both extension on the favorable side and early recovery on the constrained side.

521 4.2.3 Field monitoring of expansion deformation in the protected seam

522 Because the combined Coal Seams No. 8 and No. 9 have small interlayer spacing, soft coal, and high gas pressure,
523 borehole blowout can easily occur during drilling. For safety, field expansion-deformation monitoring was mainly
524 arranged in Coal Seam No. 9. As shown in Fig. 12d, expansion deformation began when the working face was about 18

m ahead of the measuring point. When the working face advanced to the vertical projection of the measuring point, the measured expansion deformation ratio reached 4.6 per mille. After the working face passed the measuring point by about 32 m, the expansion deformation stabilized, with a stable expansion of 40.6 mm, corresponding to an expansion deformation ratio of 19.8 per mille. This result agrees with the simulated expansion deformation peak of about 19 per mille, verifying that the model captures the main evolution process of pressure-relief deformation in the protected seam.

4.3 Dynamic characteristics and evolution of gas drainage

4.3.1 Gas-drainage characteristics during the initial mining stage

Fig. 13 shows the variation in gas-drainage rates of different drainage methods during the initial mining stage. At this stage, the working-face advance distance is short, surface boreholes have not yet fully entered the high-flow stage, and the drainage response of the protected seam has not been fully established. Goaf pipe drainage, cross-measure boreholes, conventional high-level boreholes, directional interception boreholes, and directional high-level boreholes jointly contribute to drainage. The gas sources mainly include gas emitted from the goaf, gas released from adjacent seams, and gas released by initial development of local mining-induced fractures.

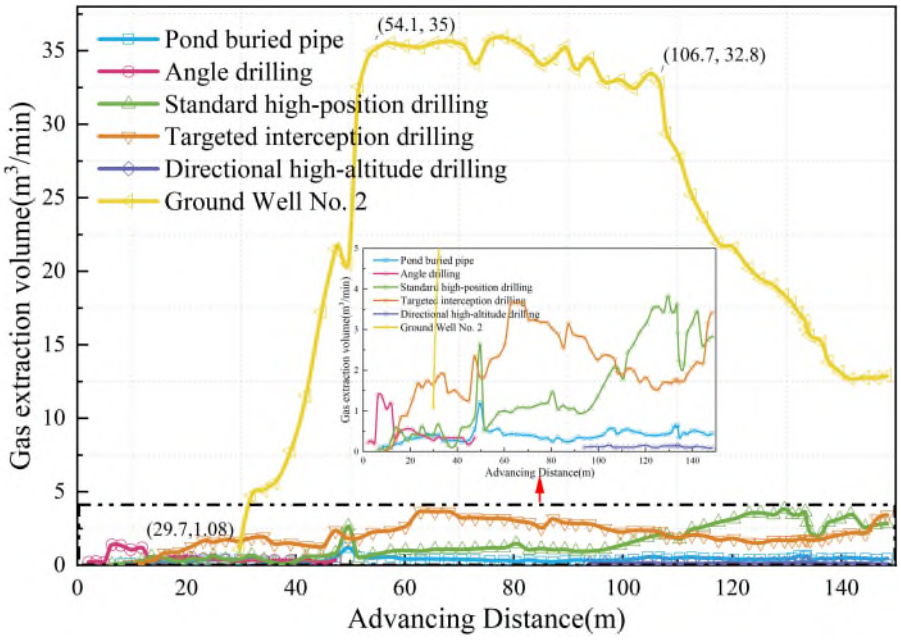


Fig. 13. Gas-drainage rates during the initial mining stage

As shown in Fig. 13, the drainage rate of goaf pipes is 0.10-0.56 m^3/min, with an average of about 0.35 m^3/min. The early drainage rate of cross-measure boreholes is relatively high and then stabilizes at 0.3-0.4 m^3/min. The drainage rate of conventional high-level boreholes is 0.06-0.63 m^3/min, with an average of about 0.40 m^3/min. Directional interception boreholes increase rapidly, reaching a maximum of 1.92 m^3/min and an average of about 1.2 m^3/min. Excluding surface boreholes, the total drainage from the mined seam and adjacent seams is about 2.1 m^3/min, the ventilation emission rate is about 3.2 m^3/min, and the total gas emission rate is about 5.3 m^3/min.

The increase in drainage rate at this stage is not drainage enhancement induced by strong pressure relief of the protected seam. Its main role is to provide information on the initial development of mining-induced fractures. In the subsequent same-scale analysis, early drainage fluctuations should not be misidentified as stable drainage enhancement of the protected seam, because this would overestimate the contribution of early mining disturbance to the drainage capacity of the protected seam.

4.3.2 Drainage response controlled by surface-borehole location and advance distance

Fig. 14 and Table 2 show that surface borehole drainage generally undergoes four stages: initial activation, high flow, competitive attenuation, and low-flow residual drainage. Surface boreholes 2#-23# are located 40-1374 m from the open-off cut and cover the main advance section of the III1022 working face. As shown in Table 2, the pressure-relief onset of each borehole occurs ahead of the borehole position, with an advance distance concentrated between 15 and 25 m and an average of about 19 m. This scale is consistent with the observation in Section 4.2.3 that expansion deformation begins when the working face is about 18 m ahead of the monitoring point. The early increase in surface-borehole flow therefore corresponds to the advance propagation of pressure-relief disturbance. Most boreholes enter the high-flow stage after the working face passes the borehole position, with lag distances of 1-28 m. Arrival of the pressure-relief disturbance does not mean that a seepage pathway has already been established. Initial pressure relief mainly changes the stress state and fracture aperture, whereas high flow requires fractures to evolve from opening to

connectivity and a stable connection to form between the mining-induced fracture network and the borehole negative-pressure field.

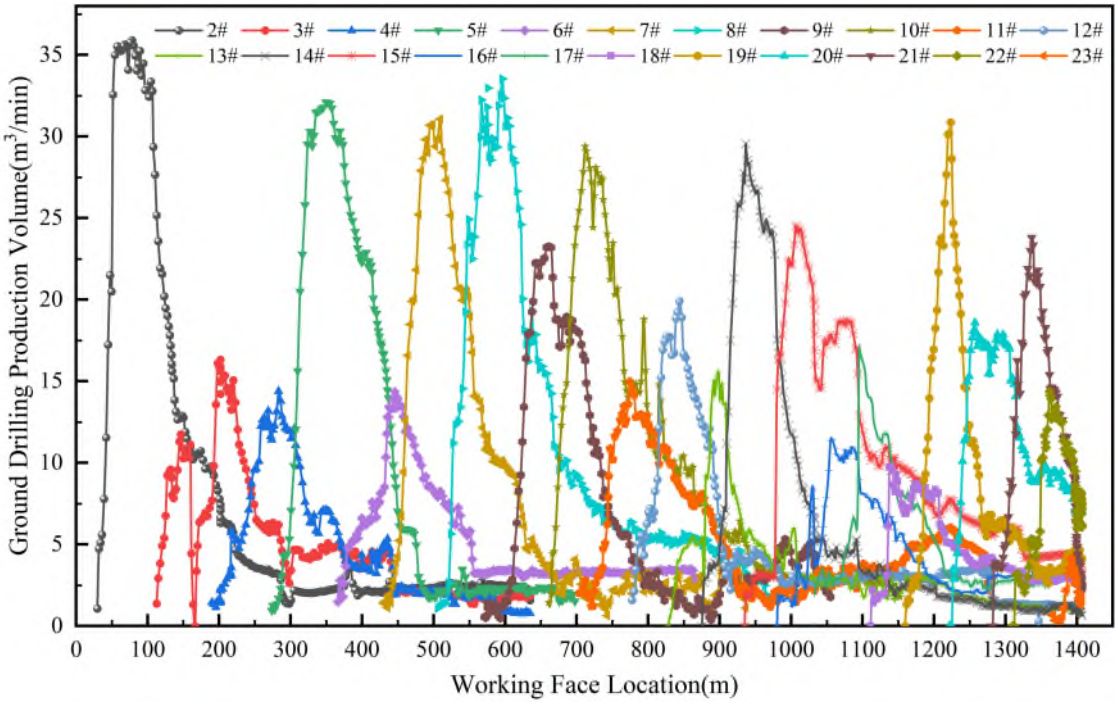


Fig. 14. Pressure-relief gas drainage performance of surface boreholes

Post-peak attenuation reflects drainage competition among boreholes. In Table 2, the average flow rates during the attenuation stage range from 3.18 to 11.79 m^3/min, showing large differences. Boreholes 20# and 21# maintain average post-peak flow rates above 10 m^3/min, indicating that good gas-source supply and flow-conducting capacity remain within their control ranges. Some boreholes quickly decrease to low flow after the peak, mainly because of local gas-source depletion, transfer of flow paths, and enhanced interception by adjacent boreholes.

Borehole spacing amplifies these differences. In the early section of the working face, adjacent boreholes are mostly spaced more than 70 m apart, and the high-flow stage of a single borehole is relatively independent. In the middle and late sections, borehole spacing decreases, and pressure-relief onset, high-flow formation, and post-peak attenuation of multiple boreholes overlap. After a subsequent borehole is activated, gas-flow paths shift toward the nearer or lower-resistance channel, and the flow of the previous borehole decreases. The drainage response is jointly controlled by borehole location, advance distance, fracture connectivity, and competition among adjacent boreholes.

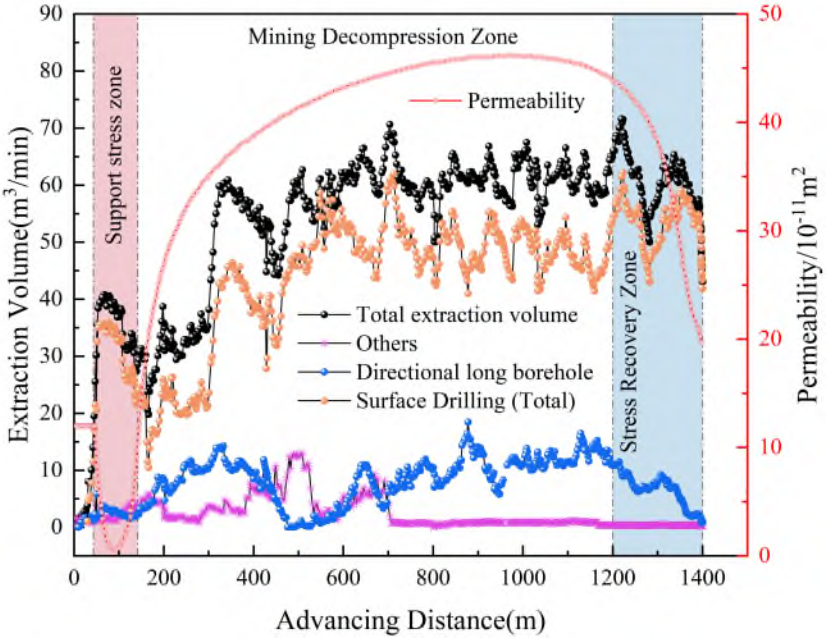
Table 2 Summary of pressure-relief and gas-drainage characteristics of surface boreholes.

No.	Distance from the open-off cut(m)	Onset position of pressure relief(m)	Advance pressure-relief distance(m)	Starting position of the high-flow stage (m)	Lag distance(m)	Attenuation parameters	
						Start position(m)	Average flow rate (m^3/min)
2#	40	19	21	41	1	180	7.54
3#	125	102	23	140	15	260	4.33
4#	205	189	16	217	12	370	4.51
5#	293	271	22	307	14	442	9.88
6#	379	360	19	410	31	552	5.02
7#	448	423	25	460	12	598	7.04
8#	523	505	18	527	4	671	10.44
9#	594	577	17	619	25	743	5.95
10#	665	645	20	676	11	850	8.53
11#	726	711	15	737	11	903	4.8
12#	784	766	18	806	20	905	4.06
13#	834	817	17	859	25	952	3.18
14#	880	864	16	905	25	1008	5.87
15#	952	927	25	980	28	1145	8.99
16#	998	983	15	1019	21	1171	4.19
17#	1055	1031	24	1081	26	1206	4.59
18#	1120	1101	19	1136	16	1226	4.42
19#	1183	1162	21	1190	7	1260	8.09
20#	1235	1217	18	1239	4	1397	10.99
21#	1298	1276	22	1305	7	1397	11.79
22#	1324	1304	20	1348	24	/	/
23#	1374	1358	16	/	/	/	/

4.3.3 Working-face-scale drainage composition and permeability evolution

Surface boreholes and other drainage methods also show a clear lag: the pressure-relief disturbance arrives ahead of the borehole position, whereas the high-flow stage forms after the working face passes the borehole. Therefore, working-face-scale analysis must address two questions: which drainage methods contribute to the total drainage rate, and how these drainage responses correspond to protected-seam pressure-relief evolution in the advance-distance

583 domain.



584

585 Fig. 15. Contributions of different gas-drainage methods and corresponding permeability evolution

586 Fig. 15 shows the contributions of different drainage methods and the corresponding permeability evolution.
587 Surface boreholes constitute the main component of the total drainage rate, directional long boreholes intercept part of
588 the mining-released gas, and the remaining methods are grouped as 'other' drainage. Before the advance distance
589 reaches 140 m, the 'other' drainage methods vary gradually, with a maximum of about 6.0 m^3/min. In the 500-700 m
590 interval, fluctuations increase and locally reach 12.84 m^3/min. After 700 m, they gradually stabilize at about 0.4 m^3/min.
591 These variations indicate that working-face-scale drainage is not a response of surface boreholes alone, but the result of
592 competition and redistribution among surface boreholes, cross-measure boreholes, directional long boreholes, and
593 goaf-related drainage methods.

594 Surface-borehole drainage generally follows the permeability evolution of the coal seam. Under front abutment
595 pressure, the coal remains compacted, and both drainage rate and permeability decrease temporarily. After the seam
596 enters the mining-induced pressure-relief zone, fracture opening and connectivity increase, permeability improves, and
597 the surface-borehole drainage rate rises accordingly. After the advance exceeds 1200 m, the fracture-matrix system
598 undergoes recompression and shrinkage and permeability decreases slowly. Nevertheless, because the original stress

field has already been reshaped by mining, the seepage capacity remains higher than the initial state and drainage stays at a relatively high level.

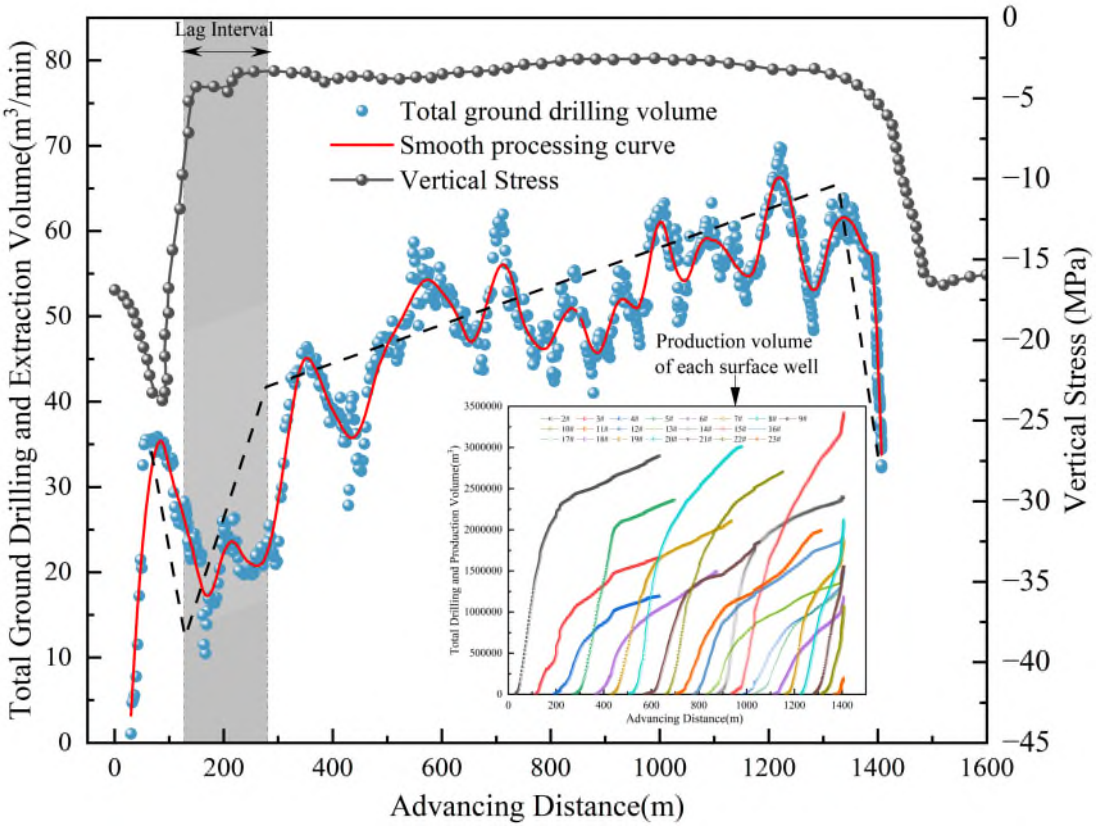


Fig. 16. Same-scale correspondence between total gas-drainage response and pressure-relief intensity in the advance-distance domain

To eliminate the influence of face-advance velocity on time-series drainage data, the total gas-drainage rate is further converted into the advance-distance function $Q(x)$ and compared on the same scale with simulated pressure-relief deformation indicators. The spatial offset in Fig. 16 is consistent with the single-borehole drainage pattern described in Section 4.3.2. At the instant of mining-induced pressure release, gas adsorbed on coal-particle surfaces begins to transform into free gas. However, high pressure and low permeability in deep coal seams produce a pronounced delay in gas desorption. As the working face advances, the migration velocity of desorbed gas is much lower than the propagation velocity of the stress disturbance. Therefore, during the early arrival of the physical pressure-relief zone, gas has not yet fully migrated from the matrix to fractures, and the response trajectory of the

612 drainage-rate peak lags markedly behind the stress-drop curve.

613 4.4 Quantitative criterion for pressure-relief-drainage coupling

614 Section 2 established the initial compaction compensation ratio $C_n(x)$ from the normal roof-floor separation of the
615 protected seam, the initial normal stress, and the equivalent compression stiffness of the coal. Based on this framework,
616 the formation position of strong pressure relief is defined as the advance distance at which $C_n(x)$ first reaches 1:

617
$$x_p = \min\left\{x \middle| \ C_n(x) \geq 1\right\} \tag{17}$$

618 where x_p is the formation position of strong pressure relief. This definition is jointly determined by the initial
619 compaction state of the coal seam and the degree of mining-induced release. For discrete advance-distance data, if
620 $C_n(x_i)<1$ and $C_n(x_{i+1})>=1$, x_p can be obtained by linear interpolation:

621
$$x_p = x_i + \frac{1-C_n(x_i)}{C_n(x_{i+1})-C_n(x_i)}\left(x_{i+1}-x_i\right) \tag{18}$$

622 The continuous strong pressure-relief interval is expressed as:

623
$$I_p = \left\{x \middle| \ C_n(x) \geq 1\right\} \tag{19}$$

624 The drainage-side input is the working-face-scale total drainage rate $Q(x)$ obtained after the same-scale
625 transformation in Section 2. Section 4 has shown that $Q(x)$ is jointly controlled by fracture connectivity, pressure
626 gradient, gas-source supply, and borehole interception capacity. Therefore, the onset of drainage enhancement
627 should not be determined using a fixed flow-rate threshold or a fixed normalized threshold. This study uses a
628 continuous piecewise-growth model to identify the change point at which $Q(x)$ shifts from a low-growth stage to a
629 sustained-growth stage.

630 A continuous piecewise linear model is constructed for the smoothed total drainage rate $Q(x)$:

631
$$\hat{Q}(x;\xi) = a + b_0 x + b_1 (x-\xi)_+ \tag{20}$$

632 where:

633
$$(x-\xi)_+ = \begin{cases} 0, & x \le \xi \\ x-\xi, & x > \xi \end{cases} \tag{21}$$

634 where x_i is the candidate change point, b_0 is the pre-change-point drainage growth rate, and b_0+b_1 is the
635 post-change-point growth rate.

636 The conditions $b_1>0$ and $b_0+b_1>0$ indicate that the drainage rate enters a sustained-growth stage after the
637 change point.

638 The candidate change point is determined by minimizing the weighted residual sum of squares:

639
$$x_q = \arg\min_{\xi} \left[\min_{a,b_0,b_1} \sum_{i=1}^{m} w_i \left(Q_i - \hat{Q}(x_i;\xi) \right)^2 \right] \tag{22}$$

640 where x_i is the advance distance corresponding to the drainage record, Q_i is the total drainage rate at that
641 advance distance, and w_i is the data weight. If the reliability of all measurement points is similar, w_i can be set to
642 1.

643 To avoid misidentifying ordinary linear growth as a stage transition, the Bayesian information criterion is
644 further used to test whether the piecewise model outperforms a single linear model:

645
$$\mathrm{BIC} = m \ln\left(\frac{\mathrm{RSS}}{m}\right) + k \ln m \tag{23}$$

646 where RSS is the residual sum of squares, k is set to 4 for the continuous piecewise model, and m is the
647 number of data points. The piecewise model is accepted only when it satisfies:

648
$$\mathrm{BIC}_{\mathrm{seg}} < \mathrm{BIC}_{\mathrm{lin}}, \qquad b_1 > 0, \qquad b_0 + b_1 > 0 \tag{24}$$

649 x_q is then identified as the working-face-scale onset of drainage enhancement.

650 The advance-distance lag between formation of strong pressure relief and manifestation of drainage
651 enhancement is therefore:

652
$$L_{pq} = x_q - x_p \tag{25}$$

653 When $L_{pq}>0$, strong pressure relief forms before drainage enhancement. When $L_{pq}=0$, the two are essentially

synchronous in the advance-distance domain.

When L_{pq}<0, background drainage fluctuations, drainage-system switching, or errors in time-to-advance-distance conversion should be checked.

To further evaluate which intervals within the strong pressure-relief zone effectively convert into drainage growth, the positive growth component of the drainage rate is extracted:

$$G_Q^+(x) = \max\left[\frac{dQ(x)}{dx}, 0\right] \tag{26}$$

where G_Q^+(x) rηins only the component in which the drainage rate increases with advance distance. If the coal seam has reached the strong pressure-relief condition but the drainage rate is stable or decreasing, that interval is not counted as a drainage-growth contribution.

The lag-corrected local conversion intensity is defined as:

$$D_{pq}(x) = C_n^+(x) G_Q^+(x + L_{pq}) \tag{27}$$

where $D_{pq}(x)$ requires two conditions: first, the coal seam must reach the initial compaction compensation level; second, after correction for the lag distance, the drainage rate must remain in a positive-growth stage.

For any advance-distance window Wk=[a_k,b_k], the cumulative conversion intensity is:

$$\Omega_k = \int_{a_k}^{b_k} D_{pq}(x)dx \tag{28}$$

The window contribution ratio is:

$$\eta_k = \frac{\Omega_k}{\sum_{j=1}^{r} \Omega_j} \times 100\% \tag{29}$$

where r is the number of effective windows included in the statistics. A high η_k indicates that the interval has both a high initial compaction compensation margin and sustained drainage growth, and is therefore a preferred interval for conversion from strong pressure relief to drainage enhancement. A low η_k indicates that the interval may satisfy the strong pressure-relief condition, but drainage growth is strongly affected by fracture-connectivity

quality, gas-source supply, inter-borehole competition, or local recompaction.

4.5 Application of the evaluation method and inversion of drainage lag distance

According to the FLAC^{3D} simulation results for the III1022 working face, the roof-floor relative displacement of the protected seam was extracted, and the initial compaction compensation ratio $C_n(x)$ was calculated using the method established in Section 2. The results show that the advance distance at which $C_n(x)$ first reaches 1 is:

$$x_p = 128.8\ \text{m} \tag{30}$$

The continuous strong pressure-relief interval is:

$$I_p = [128.8, 1216.6]\ \text{m} \tag{31}$$

Therefore, before the working face advances to 128.8 m, the mining-induced released deformation of the protected seam has not yet reached the initial compaction compensation level. After 128.8 m of advance, the protected seam satisfies the mechanical release condition required for strong pressure-relief formation. This position is determined jointly by the initial stress state, equivalent compression stiffness, seam thickness, and normal roof-floor separation, thereby avoiding the case dependence of a fixed absolute expansion-deformation threshold.

After the field total drainage rate is transformed into the advance-distance domain, $Q(x)$ is analyzed using the continuous piecewise-growth identification method in Eqs. (20)-(24). The results show that the piecewise model satisfies the condition of an increased slope after the change point, and the position at which the total drainage rate shifts from a low-growth stage to a sustained-growth stage is:

$$x_q = 280.4\ \text{m} \tag{32}$$

This position indicates the onset of sustained enhancement in the working-face-scale total drainage rate. Compared with a fixed normalized drainage threshold, the piecewise-growth change point is determined directly from the slope variation of the drainage curve and reduces the influence of subjective thresholds on identifying the onset of drainage enhancement.

From Eq. (25), the advance-distance lag between formation of strong pressure relief and manifestation of drainage enhancement is:

$$L_{pq} = x_q - x_p = 280.4 - 128.8 = 151.6 \text{ m} \tag{33}$$

C_n>=1 indicates volumetric expansion of the coal mass, but this stage represents only the generation of microfractures. According to percolation theory, isolated microfractures interconnect only after the advance distance reaches a critical point, forming a stable and throughgoing seepage network. The 151.6 m offset is therefore the evolutionary distance required for the microfracture network to evolve from disordered initiation to ordered connectivity.

The inversion result can be used to distinguish the dominant causes of insufficient drainage. When a given interval satisfies $C_n(x)$<1, weak drainage is mainly controlled by insufficient mining-induced release. When $C_n(x)$>=1 but the interval has not yet entered the sustained-growth stage after x_q, the coal seam has reached the strong pressure-relief condition, and insufficient drainage is more likely controlled by fracture connectivity, inter-borehole competition, local gas-source depletion, or drainage-system efficiency.

In summary, for the III1022 working face, the formation position of strong pressure relief is 128.8 m, the continuous strong pressure-relief interval is 128.8-1216.6 m, and the onset of working-face-scale drainage enhancement is 280.4 m, giving an advance-distance lag of 151.6 m. Protective seam mining first changes the initial compaction state of the protected seam, allowing the coal mass to reach the strong pressure-relief condition. Subsequently, fracture connectivity, pressure-field adjustment, gas-source mobilization, and drainage-system interception jointly control the position where drainage enhancement appears. The proposed initial-compaction-compensation and drainage-growth change-point method has a clear mechanical basis and statistical identification framework and can be used to determine the effective pressure-relief range, drainage initiation timing, and drainage lag distance under different mining conditions.

5 Discussion

5.1 Mechanism of drainage lag

The results in Section 4 show that the formation position of strong pressure relief in the protected seam is x_p=128.8 m, the onset of working-face-scale drainage enhancement is x_q=280.4 m, and the corresponding lag distance is L_{pq}=151.6 m. This result indicates that, after the protected seam reaches the initial compaction compensation level, the working-face-scale total drainage rate does not immediately enter a sustained-growth stage.

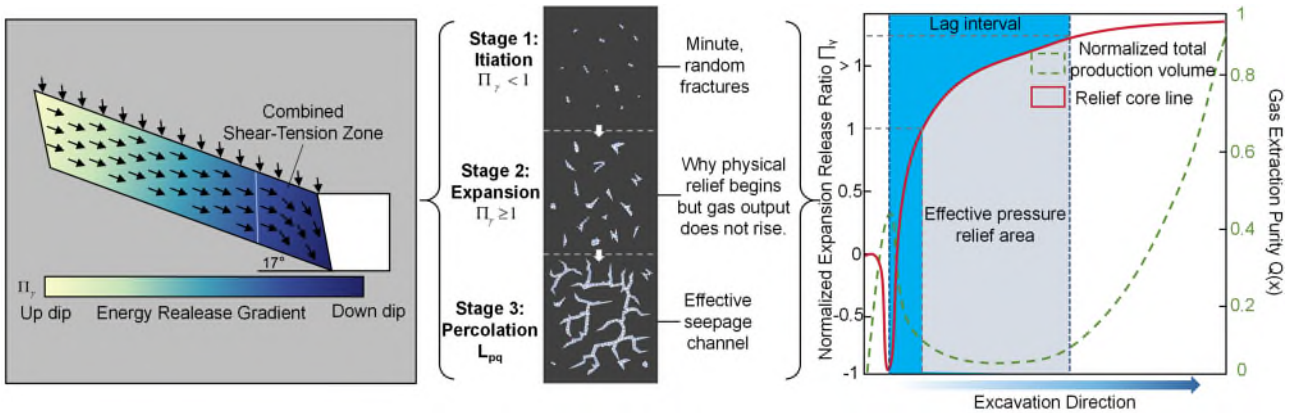


Fig. 17. Conceptual mechanism of the spatially lagged transformation from pressure relief to effective gas drainage in a deep inclined protected seam.

The spatial lag mechanism for the conversion from strong pressure relief to effective drainage is shown in Fig. 17. In inclined coal seams, mining-induced pressure relief does not develop symmetrically. The down-dip side is more favorable for combined shear-tensile failure, has a stronger release gradient, and allows the strong pressure-relief zone to expand more readily toward that side. This asymmetric structure controls the initial pressure-relief range and determines the preferential direction of subsequent fracture development. Fracture evolution can be divided into three stages. The first is the compaction-constrained stage, where $C_n(x)$<1, mining-induced released deformation has not compensated the initial normal compaction strain, and only scattered microfractures occur within the coal mass. The second is the expansion-release stage, where $C_n(x)$>=1 and the protected seam satisfies the strong pressure-relief condition, but fractures remain locally opened and discontinuously propagated and cannot yet support stable drainage.

737 The third is the connected-flow stage, where the fracture network establishes effective communication with the drainage
738 negative-pressure field, continuous seepage channels form, and the working-face-scale total drainage rate $Q(x)$ enters a
739 sustained-growth stage.

740 The curve on the right gives the physical meaning of L_{pq}. The pressure-relief indicator $C_n(x)$ first reaches the
741 critical condition, and the drainage response $Q(x)$ enters sustained growth later. The distance between xp and x_q is not a
742 calculation error, but the spatial maturation distance required for fracture connectivity, pressure-gradient reorganization,
743 gas-source mobilization, and borehole interception capacity to develop. Therefore, the strong pressure-relief boundary
744 and the drainage-enhancement boundary must be identified separately.

745 5.2 Robustness test based on the spatial distribution of coupling intensity

746 The continuous strong pressure-relief interval is I_p=[128.8,1216.6] m, but the drainage conversion intensity is not
747 uniformly distributed within this interval. According to Eqs. (27)-(29), the local conversion intensity $D_{pq}(x)$ is jointly
748 controlled by the initial compaction compensation margin C_n^+(x) and the lag-corrected positive drainage-growth
749 component $G_Q^+(x+L_{pq})$. An interval contributes to conversion intensity only when the coal seam satisfies the strong
750 pressure-relief condition and the drainage rate remains in a positive-growth stage.

751 Table 3 Contributions of individual activation windows to cumulative synergy intensity

Interval	Start position （m）	End position （m）	Ω_k	Contribution ratio （%）	Length （m）
I1	130.9	151.6	5.851	3.663	21.9
I2	236	373.6	50.599	31.677	137.6
I3	455.6	509.9	23.149	14.492	54.3
I4	589	637.1	11.527	7.217	48.1
I5	688.8	733.8	14.099	8.827	45.0
I6	758	801.8	21.457	13.433	43.8
I7	847.4	885.2	9.459	5.922	37.8
I8	964.2	1019.9	16.799	10.517	55.7
I9	1084.4	1137.1	6.795	4.254	52.7

752 Table 3 and Fig. 18 show that the lag-corrected cumulative conversion intensity is concentrated in a few intervals.
753 Interval I_2 has the highest contribution ratio, 31.68%; the contribution ratios of I_3, I_6, and I8 are 14.49%, 13.43%, and

10.52%, respectively. These four windows together contribute about 60.12%, indicating that drainage conversion within the strong pressure-relief zone is not continuous or uniform, but concentrated in intervals where fracture connectivity, gas-source conditions, and borehole interception are well matched.

Even if an interval is relatively long, its cumulative conversion contribution may remain low when drainage growth has slowed or has been weakened by borehole competition. Although I_9 has a contribution length of 52.7 m, its contribution ratio is only 4.254%, further indicating that late-stage drainage growth within the strong pressure-relief zone is affected by attenuation and flow-field redistribution.

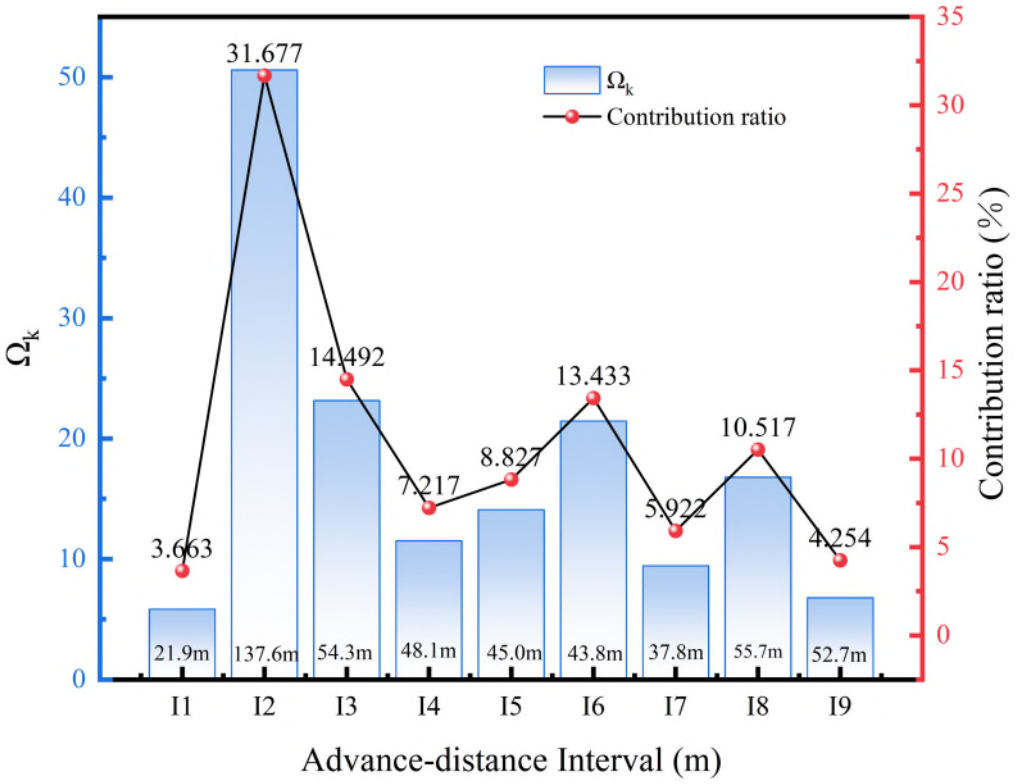


Fig. 18. Distribution of local conversion intensity $D_{pq}(x)$ and contributions of individual activation interval.

After the protected seam reaches the strong pressure-relief condition, drainage-conversion efficiency may still decline because of gas-source depletion, borehole diversion, local recompression, and weakening of the pressure gradient. The strong pressure-relief interval can therefore be divided into high-conversion, weak-conversion, and low-efficiency conversion segments. High-conversion segments correspond to positions with favorable fracture connectivity and gas desorption conditions; weak-conversion segments usually occur during drainage-growth

attenuation; and low-efficiency segments may be limited by insufficient local flow channels or drainage competition. Thus, working-face-scale drainage lag is not caused by a single positional offset but is composed of multiple local conversion windows. Strong pressure relief provides the necessary mechanical basis, whereas drainage enhancement is governed by fracture-network maturity, gas-source mobilization, and drainage-system configuration.

5.3 Robustness tests for mechanical and drainage parameters

The formation position of strong pressure relief and the onset of drainage enhancement identified in Section 4 are x_p=128.8 m and x_q=280.4 m, respectively, corresponding to a lag distance of L_{pq}=151.6 m. Because xp is derived from the normalized expansion-release ratio $C_n(x)$, whereas xq is derived from piecewise-growth identification of the total drainage rate $Q(x)$, their uncertainty sources differ. To avoid misinterpreting a result caused by parameter selection or data processing as physical lag, this section evaluates robustness from both the mechanical and drainage sides.

Mechanical-side uncertainty mainly arises from roof-floor separation, seam thickness, initial normal stress, equivalent compression modulus, and seam dip angle. The governing relation is:

$$C_n(x) = \frac{\gamma_n(x)}{\varepsilon_{n0}} = \frac{\gamma_n(x) M_c}{\sigma_{n0}} \tag{34}$$

When the vertical roof-floor displacement difference is used with dip-angle correction, $C_n(x)$ can be interpreted as the combined result of mining-induced released strain, seam thickness, coal stiffness, and the initial compaction state. To characterize the influence of these input parameters on x_p, the perturbed normalized expansion-release ratio is written as:

$$C_n^*(x) = \lambda C_n(x) \tag{35}$$

$$\lambda = \lambda_{\Delta h} \lambda_{h_s}^{-1} \lambda_{M_c} \lambda_{\sigma}^{-1} \frac{\cos\theta_0}{\cos\theta} \tag{36}$$

where $\lambda_{\Delta h}$、λ_{hs}、λ_{Mc}, and λ_{σ} are the perturbation coefficients for roof-floor separation, seam thickness, equivalent compression modulus, and initial normal stress, respectively, and θ_0=17 deg is the reference seam dip angle.

Fig. 19a shows the 2.5%, 50%, and 97.5% percentile curves of 800 sets of $C_n(x)$ under parameter perturbation,

790 together with the baseline curve and the critical criterion C_n=1. Although the percentile curves show some amplitude
791 differences in the middle and late advance stages, they all rise steeply near the onset of strong pressure relief and cross
792 C_n=1 at approximately x=128.8 m. This indicates that identification of the strong pressure-relief onset is controlled
793 mainly by the early rapid-growth segment of $C_n(x)$, rather than by amplitude fluctuations of $C_n(x)$ in the middle and late
794 stages. Even with input-parameter uncertainty, the position where $C_n(x)$ first reaches the initial compaction
795 compensation level remains stable.

796 Fig. 19b shows the direction and magnitude of the effects of positive and negative perturbations of each input
797 parameter on the baseline $C_n(x)$ result. The one-at-a-time sensitivity results show that the initial normal stress σ_{n0} and
798 the equivalent compression modulus M_c have the strongest effects on $C_n(x)$. The reason is:
799

$$C_n(x) \propto \frac{M_c}{\sigma_{n0}} \tag{37}$$

800 When M_c increases, the initial compaction strain decreases and $C_n(x)$ increases. When σ_{n0} increases, the initial
801 compaction strain increases and $C_n(x)$ decreases. Seam thickness hs and roof-floor separation Δh also affect $C_n(x)$:
802 increasing Δh increases expansion release, whereas increasing h_s reduces the equivalent expansion deformation ratio per
803 unit thickness. In comparison, perturbation of the seam dip angle has the weakest effect.θ

804 Fig. 19c further shows the distributions of the input parameters used in the Monte Carlo analysis. Roof-floor
805 separation Δh and seam thickness h_s are perturbed slightly around their baseline values, whereas the perturbation ranges
806 of equivalent compression modulus M_c and initial normal stress σn0 are relatively wider. All parameter perturbations are
807 distributed around their baseline values, indicating that the sensitivity analysis tests the stability of x_p within
808 engineeringly reasonable parameter ranges rather than under extreme parameter combinations.

809 Fig. 19d shows the output distributions of x_p, the terminal position of the strong pressure-relief zone, and L_{pq}. The
810 results show that the confidence interval of x_p is concentrated within [127.9,129.5], with a fluctuation of less than 1 m
811 relative to the baseline value. The distribution range of x_q is [1178.0,1238.6], indicating that mechanical-parameter

perturbations have a more pronounced effect on the rear boundary and length of the strong pressure-relief interval. By contrast, the distribution of L_{pq} is [150.9,152.5], remaining tightly centered around the baseline value. This result indicates that mechanical-side parameter perturbations mainly affect the rear boundary of the strong pressure-relief zone and do not change the basic relationship that strong pressure relief forms before drainage enhancement.128.8 m151.6 m

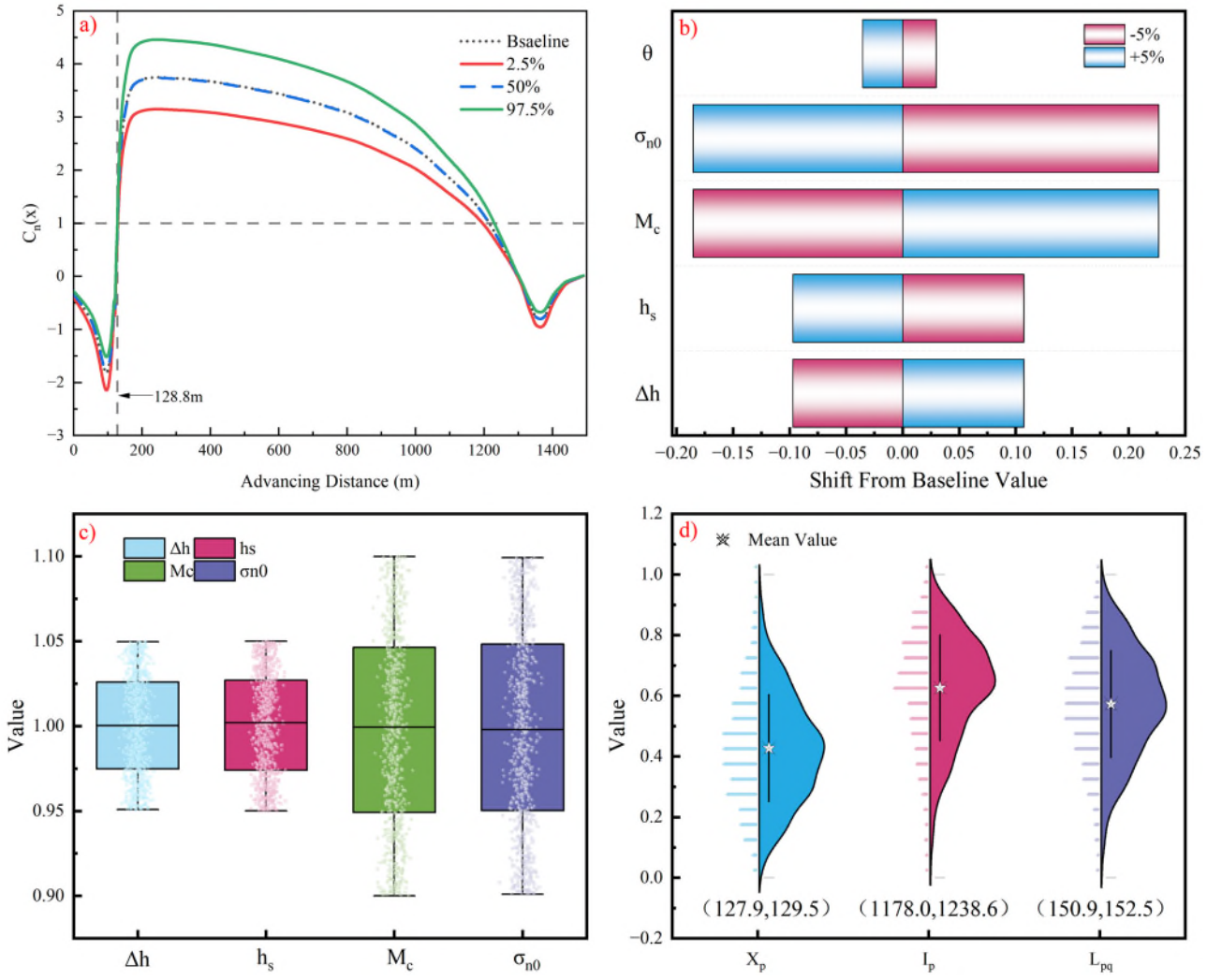


Fig. 19. Mechanical-side uncertainty analysis for identifying the pressure-relief onset: (a) percentile curves of $C_n(x)$ under parameter uncertainty; (b) one-at-a-time sensitivity of input parameters; (c) distributions of perturbed input parameters; and (d) output distributions of x_p, the terminal position of I_p, and L_{pq}.

Drainage-side uncertainty mainly arises from $Q(x)$ data processing and change-point identification. The working-face-scale total drainage rate is the superposed response of multiple surface boreholes and other drainage

channels, and local flow fluctuations, borehole competition, negative-pressure adjustment, and gas-source allocation may all affect the shape of the drainage curve. If the smoothing scale is too small, local operational fluctuations may be misidentified as a growth change point; if the smoothing scale is too large, the real growth transition may be delayed. Therefore, this study further tests the stability of x_q identification using different smoothing methods and fitting-window combinations.

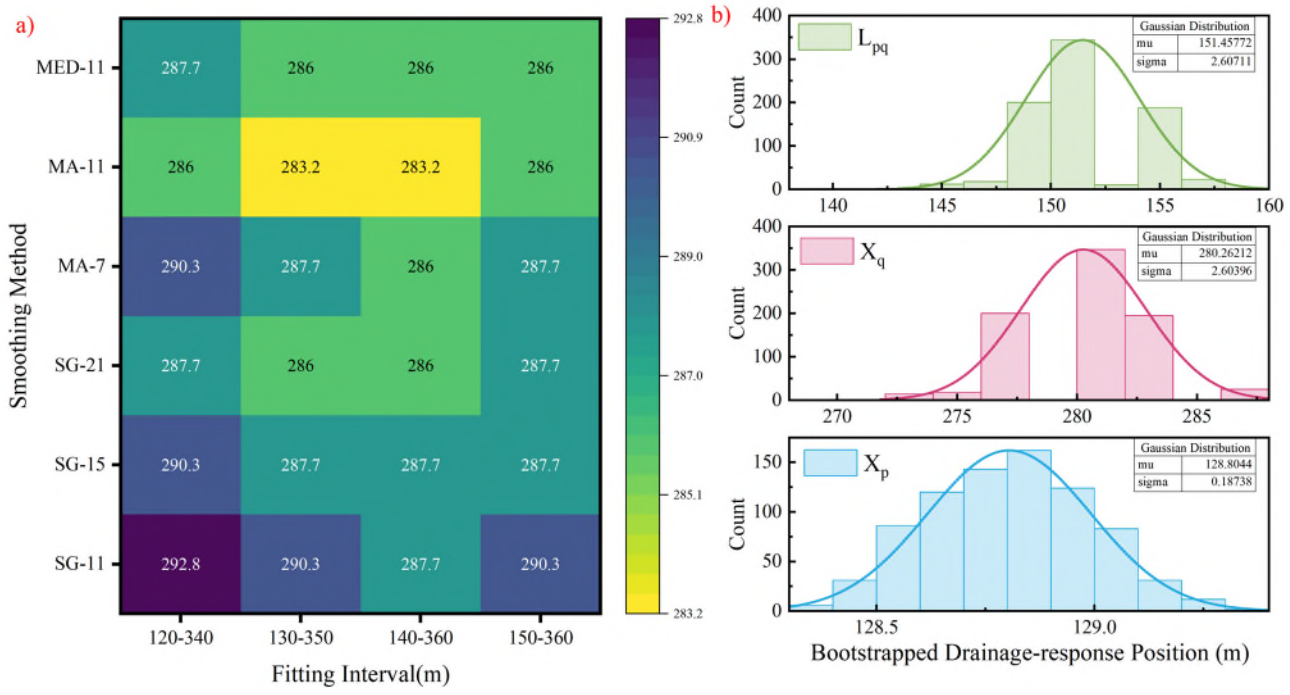


Fig. 20. Drainage-side robustness of the inferred drainage-response position: (a) inferred x_q under different smoothing methods and fitting interval; and (b) Bootstrap distributions and Gaussian fits of L_{pq}, x_q, and x_p.

Fig. 20a shows the drainage-enhancement onset x_q identified using different smoothing and fitting methods. The smoothing methods include Savitzky-Golay smoothing, moving-average smoothing, and median filtering, and the fitting windows are 120-340 m, 130-350 m, 140-360 m, and 150-360 m. The identified x_q values are mainly distributed within [283.2,292.8]. The minimum value, 283.2 m, occurs under 11-point moving-average smoothing, whereas the maximum value, 292.8 m, occurs under 11-point Savitzky-Golay smoothing with the 120-340 m fitting window. Different smoothing and fitting-window settings therefore shift x_q by several to more than ten meters, but all identified

836 positions remain after the strong pressure-relief formation position x_p and do not change the conclusion that drainage
837 enhancement lags behind strong pressure-relief formation.

838 Fig. 20b further presents the bootstrap distributions and Gaussian fits of L_{pq}, x_q, and x_p. The distribution of x_p is the
839 most concentrated, with a mean of about 128.8 m and small dispersion. The distribution range of x_q is relatively wider,
840 with a mean near 280 m, indicating that change-point identification of the drainage curve has greater data-processing
841 uncertainty than identification of the mechanical-side strong pressure-relief onset.

842 Taken together, Figs. 19 and 20 show that the strong pressure-relief onset x_p is insensitive to mechanical
843 input-parameter perturbations, mainly because $C_n(x)$ crosses the C_n=1 criterion steeply near the onset. The
844 drainage-enhancement onset x_q is more sensitive to smoothing method and fitting window, but the identified results
845 under different treatments remain within 300 m and consistently occur well after x_p.

846 Mechanistically, $C_n(x)$>=1 indicates only that the mining-induced released deformation of the protected seam has
847 reached the initial compaction compensation level and that the coal mass has the mechanical basis for sustained fracture
848 propagation and structural relaxation. Sustained growth of $Q(x)$, however, further requires fracture connectivity, stable
849 flow channels, pressure-gradient reorganization, and effective interception by the drainage system. Therefore, an
850 advance-distance lag between strong pressure-relief formation and drainage-enhancement manifestation is reasonable.
851 Figs. 18 and 19 confirm that this lag relationship remains stable under both mechanical-side parameter perturbations
852 and drainage-side data-processing perturbations.

853 # 6 Conclusions

854 Taking the III1022 working face of Luling Coal Mine as the engineering background, this study integrates FLAC^{3D}
855 numerical simulation, field verification of pressure-relief boundaries, roof-floor deformation monitoring, and
856 surface-borehole drainage data to establish a same-scale pressure-relief-drainage analysis method based on
857 working-face advance distance. The main conclusions are as follows:

(1) After deep lower protective seam mining, the mining-induced response of the protected seam shows clear spatial zoning and staged evolution. Along strike, it is characterized by front stress concentration, central strong pressure relief, and rear adjustment. Along dip, it shows asymmetric pressure relief jointly controlled by seam dip, interlayer structure, and boundary load recovery. After the strong pressure-relief zone forms, its controlling range tends to stabilize, and subsequent evolution is dominated by overall migration with the advancing working face rather than unlimited expansion with advance distance. Therefore, the mining-affected range, strong pressure-relief range, and effective drainage-enhancement range should not be treated as equivalent.

(2) By introducing the initial compaction compensation ratio $C_n(x)$, the formation of strong pressure relief in the protected seam can be quantitatively identified from the compensation degree of mining-induced released deformation relative to the initial normal compaction strain. Compared with a fixed absolute deformation threshold, $C_n(x)$ accounts for seam thickness, coal stiffness, and initial stress state, thereby reducing dependence on a single empirical threshold. In the III1022 working face, $C_n(x)$ first reaches 1 at an advance distance of x_p=128.8 m, and the continuous strong pressure-relief interval is 128.8-1216.6 m. Within this range, the protected seam has the mechanical basis for sustained fracture propagation and structural relaxation.

(3) Piecewise-growth identification of the working-face-scale total drainage rate $Q(x)$ shows that drainage enhancement is not synchronous with the formation of strong pressure relief. The position at which the total drainage rate shifts from a low-growth stage to a sustained-growth stage is x_q=280.4 m, lagging the strong pressure-relief formation position by 151.6 m. This lag reflects the spatial maturation process required for fractures to evolve from opening to connectivity, for the pressure gradient to reorganize, for gas sources to be mobilized, and for borehole interception capacity to form. The single-borehole pattern in which pressure-relief disturbance precedes high flow also supports this interpretion.

(4) The lag-corrected local conversion intensity $D_{pq}(x)$ indicates that drainage conversion within the strong

pressure-relief zone is markedly nonuniform. The cumulative conversion intensity is concentrated in a few preferential windows, among which I_2, I_3, I_6, and I_8 are the main contribution intervals. Not all positions within the strong pressure-relief zone can synchronously transform into efficient drainage response. High-contribution windows generally have a high initial compaction compensation margin, good fracture connectivity, sustained gas-source supply, and effective borehole interception capacity.

(5) Neither mechanical-side parameter perturbations nor drainage-side data-processing perturbations change the basic relationship that strong pressure relief forms before drainage enhancement. $C_n(x)$ crosses steeply near the strong pressure-relief onset, making x_p insensitive to input-parameter perturbations. Although x_q shifts under different smoothing methods and fitting windows, it remains consistently later than x_p. Therefore, L_{pq}=151.6 m is not an apparent offset caused by a single parameter choice or local drainage fluctuation, but a real spatial lag in the conversion from pressure-relief deformation to effective drainage response in deep low-permeability coal seams.

(6) The proposed same-scale $C_n(x)$-$Q(x)$ evaluation method can distinguish between two problems: failure to form strong pressure relief and insufficient drainage conversion after strong pressure relief has formed. When $C_n(x)<1$, insufficient drainage is controlled mainly by inadequate mining-induced release. When $C_n(x)>=1$ but $Q(x)$ has not entered a sustained-growth stage, diagnosis should focus on fracture connectivity, gas-source supply, inter-borehole competition, negative-pressure allocation, and borehole sealing quality. This method provides a quantitative basis for determining the effective protection range, optimizing drainage initiation timing, and treating low-efficiency drainage intervals in deep coal seam groups.

References

[1] Yuan L,Zhang T,Wang Y, et al. Scientific problems and key technologies for safe and efficient mining of deep coal resources. Journal of China Coal Society, 2025, 50(1): 1−12. doi:10.13225/j.cnki.jccs.YG25.0016

[2] IEA (2024), Coal 2024, IEA, Paris https://www.iea.org/reports/coal-2024, Licence: CC BY 4.0

[3] Peng X, Qi L, Wang Z, Zhou X, Hua C. Study on overburden movement deformation and roof breakage law of under-protective steeply inclined coal seam mining. Sustainability. 2022;14(16). doi:10.3390/su141610068

[4] Ren D, Xian X. Distribution of roof pressure in front of and behind the working face. Journal of China Coal Society. 1980;(2):44-50. doi:10.13225/j.cnki.jccs.1980.02.004

[5] Xue J, Xiao J, Du X,et al. Current situation and development trend of pressure-relief gas pressure relief in the protective layer mining in coal mines in China. Coal Geology & Exploration, 2023,51(6):50−61. doi:10.12363/issn.10011986.22.11.0894

[6] Chen X, Chen X, Hu J, et al. Mechanism and quantitative traceability of anomalous outflow of unloaded gas from protective layer mining under complex tectonics. Journal of China Coal Society, 2025;50(5):2509-2526. doi:10.13225/j.cnki.jccs.2024.0782

[7] Wang D, Wei J, Wen Z, et al. Numerical simulation and water inrush risk evaluation for lower protective seam mining. Journal of Chongqing University. 2013;36(9):64-70. doi:10.11835/j.issn.1000-582X.2013.09.010

[8] Xu C, Ma S, Wang K, et al. Stress and permeability evolution of high-gassy coal seams for repeated mining. Energy. 2023;284:128601. doi:10.1016/j.energy.2023.128601

[9] Lu A, Song D, Li Z, et al. Numerical simulation study on pressure-relief effect of protective layer mining in coal seams prone to rockburst hazard. Rock Mech Rock Eng. 2024;57(8):6421-6440. doi:10.1007/s00603-024-03826-5

[10] Zhu Z, Xie J, Zhang Y, et al. Mining-induced fracture network reconstruction and anisotropic mining-enhanced permeability evaluation using fractal theory. Journal of Rock Mechanics and Geotechnical Engineering. 2025;17(4):2256-2275. doi:10.1016/j.jrmge.2024.05.039

[11] Zhao Y, Zhao Y, Liu J, Wei M, Zhao Z, Elsworth D. Why does coal permeability time dependency matter? Fuel. 2025;381:133373. doi:10.1016/j.fuel.2024.133373

[12] Yin G, Li M, Wang J, Xu J, Li W. Mechanical behavior and permeability evolution of gas infiltrated coals during protective layer mining. Int J Rock Mech Min Sci. 2015;80:292-301. doi:10.1016/j.ijrmms.2015.08.022

[13] Bai X, Wang Y, He G, et al. Research on a permeability model of coal damaged under triaxial loading and unloading. Fuel. 2023;354:129375. doi:10.1016/j.fuel.2023.129375

[14] Jing S, Zhao H, Liu C, et al. Effect of triaxial stress on permeability and enhancement rate of coal seams: Implications for gas extraction efficiency. Physics of Fluids. 2025;37:022014. doi:10.1063/5.0250782

[15] Rong T, Liu P, Wang J, Ren X, Li X, Wang G. Evolution of permeability and gas seepage in deep coal under 3d stress. Nat Resour Res. 2024;33(2):765-791. doi:10.1007/s11053-023-10306-0

[16] Zhang J, Hou X, Liu S, et al. Quantifying and modeling of coal permeability spatiotemporal response: Implications for gas recovery and CO2 sequestration. Fuel. 2025;388:134561. doi:10.1016/j.fuel.2025.134561

[17] Yang M, Wang M, Wang Y, Zhang J, Zhang L, Wang Z. Coal pore structure changes in upper protective seam after

mining: Pingdingshan Shenma Group, Henan Province, China. Journal of Petroleum Science and Engineering. 2022;218:111045. doi:10.1016/j.petrol.2022.111045

[18] Wang L, Lu Z, Chen D peng, et al. Safe strategy for coal and gas outburst prevention in deep-and-thick coal seams using a soft rock protective layer mining. Saf Sci. 2020;129. doi:10.1016/j.ssci.2020.104800

[19] Jin K, Cheng Y, Wang W, et al. Evaluation of the remote lower protective seam mining for coal mine gas control: A typical case study from the Zhuxianzhuang Coal Mine, Huaibei Coalfield, China. J Nat Gas Sci Eng. 2016;33:44-55. doi:10.1016/j.jngse.2016.05.004

[20] Wang J, Wang X. Seepage characteristic and fracture development of protected seam caused by mining protecting strata. Journal of Mining and Strata Control Engineering, 2021,3(3):033511. doi:10.13532/j.jmsce.cn10-1638/td.20201215.001

[21] Kan Z, Zhang L, Liu X, et al. Coal permeability evolution under coupled mining disturbance and gas extraction conditions: An experimental study. Natural Gas Industry B. 2025;12(5):607-622. doi:10.1016/j.ngib.2025.09.005

[22] Zhao D, Chang H, Pu Y, et al. Study on mechanical parameters and creep seepage characteristics of different coal and rock combination samples. Geomech Geophys Geo-energ Geo-resour. 2023;9(1):25. doi:10.1007/s40948-023-00569-5

[23] N. Danesh N, Chen Z, Connell LD, et al. Characterisation of creep in coal and its impact on permeability: An experimental study. International Journal of Coal Geology. 2017;173:200-211. doi:10.1016/j.coal.2017.03.003

[24] Wang J, Yang S, Qi Y, et al. Creep characteristics and damage model of coal–rock combinations with different height ratios. Scientific Reports. 2023;13(1):23072. doi:10.1038/s41598-023-49841-4

[25] Lv K, Zhang H, Wu B, et al. Damage constitutive model and experimental study of deep coal rock under thermal-hydro-mechanical coupling. Scientific Reports. 2025;15(1):29337. doi:10.1038/s41598-025-10728-1

[26] Cai Y, Wang K, Yuan L, et al. Numerical simulation and verification of unloading damage evolution characteristics of coal and rock mass during deep mining. Journal of China Coal Society, 2019,44(5) :1527-1535. doi:10.13225/j.cnki.jccs.2019.6004

[27] Liu Y, Wei K, Wang A, et al.. Dynamic permeability response and pore-fracture structure evolution of deep coal reservoirs under stress release. Nat Resour Res. 2025;34(2):953-982. doi:10.1007/s11053-024-10418-1

[28] Ye D, Liu G, Lin X,et al.. Evaluating damage growth and outburst trend during gas drainage under coupled microstructure-multi-field behaviour. Rock Mech Rock Eng. 2025;58(2):1671-1692. doi:10.1007/s00603-024-04217-6

[29] Wang Z, Feng R, Gao Y, et al. Research on mining technology of nether protectiveseamin inclined contiguous

964 seams with continuouspressure-relief on outburst coal seam. Chinese Journal of Rock Mechanics and Engineering,
965 2013;32(S2):3795-3803
966 [30] Sun H, Fan C, Yang L, et al. Modelling of enhanced gas extraction in low permeability coal seam by controllable
967 shock wave fracturing. Scientific Reports. 2024;14(1):24155. doi:10.1038/s41598-024-74259-x
968 [31] Wei M, Liu C, Liu Y, et al. Long-term effect of desorption-induced matrix shrinkage on the evolution of coal
969 permeability during coalbed methane production. Journal of Petroleum Science and Engineering. 2022;208:109378.
970 doi:10.1016/j.petrol.2021.109378
971 [32] Harpalani S, Chen G. Estimation of changes in fracture porosity of coal with gas emission. Fuel.
972 1995;74(10):1491-1498. doi:10.1016/0016-2361(95)00106-F
973 [33] Cao W, Lei Q, Cai W. Stress-Dependent deformation and permeability of a fractured coal subject to
974 excavation-related loading paths. Rock Mech Rock Eng. 2021;54(8):4299-4320. doi:10.1007/s00603-021-02520-0
975 [34] Liu J, Qin Y, Zhang S, He C. Numerical solution for borehole methane flow in coal seam based on a new
976 dual-porosity model. Journal of Natural Gas Science and Engineering. 2019;68:102916.
977 doi:10.1016/j.jngse.2019.102916
978
979
980 **Funding statement:** This research received no external funding.